Ocean Engineering 269 (2023) 113464

Contents lists available at ScienceDirect

Ocean Engineering

journal homepage: www.elsevier.com/locate/oceaneng

Study on wave slamming characteristics of a typical floating wind turbine under freak waves

Fali Huo [a], Yupeng Zhao [a], Jingxi Zhang [a], Ming Zhang [b], Zhi-Ming Yuan [b,*]

[a] School of Naval Architecture and Ocean Engineering, Jiangsu University of Science and Technology, Zhenjiang, 212000, PR China
[b] Department of Naval Architecture, Ocean & Marine Engineering, University of Strathclyde, Glasgow, G4 0LZ, UK

ARTICLE INFO

Handling Editor: Prof. A.I. Incecik

Keywords:
CFD method
Double-peak
Experimental test
Freak wave
Slamming pressure
Typical floating wind turbine

ABSTRACT

Freak waves can cause serious damage to offshore structures because of their characteristics of high peak energy, short duration, and great contingency. In this study, the slamming pressure characteristics of a typical floating wind turbine under freak waves are studied by numerical simulation and experiment. The computational fluid dynamics (CFD) method is used to establish the numerical tank. The experimental test of a typical float wind turbine is implemented at Jiangsu University of Science and Technology. The numerical model of a floating wind turbine system is modified based on an experimental test. The slamming characteristics of a floating wind turbine under the freak wave are studied using the modified numerical model. The combined wave focusing model and the push pedal wave-making theory are adopted to simulate the freak wave. Results show that the slamming pressure of a floating wind turbine under a freak wave is much larger than that under a conventional random wave with the same significant wave height. Meanwhile, the evident phenomenon of double-peak slamming is observed in the wave slamming of the floating wind turbine. The impact period at different locations varies although the floating wind turbine is a monolithic structure.

1. Introduction

Wind power has become a more promising renewable energy because of its clean and renewable features. Considering the limited offshore space resources, a wind turbine is developed from offshore to the deep sea. Compared with offshore fixed wind turbines, floating wind turbines must overcome more severe sea conditions. Freak waves have the characteristics of large wave height, extremely fast propagation speed, sudden appearing, and strong, which can cause great damage to marine engineering structures. Given that floating wind turbines have lightweight and slender structures, the freak waves can easily threaten the safety of the wind turbine system. Therefore, studying the wave slamming characteristics of the floating wind turbine under extreme sea conditions is of great significance, particularly in freak wave conditions.

In previous studies of theory and numerical simulation, the wave slamming problem was mainly studied with the potential flow theory. Baarholm (Baarholm and Faltinsen, 2004) used three different numerical methods to solve the boundary value problem and obtained the expression of the slamming pressure at the bottom of the deck of a fixed offshore platform. Faltinsen (1990) and Jain (1997) proposed a classical model for approximate analyze the interaction between small amplitude regular waves and simple structures. However, this model was not suitable for the calculation of complex models. Therefore, Nielsen (2003) applied boundary integral method and other techniques to carry out numerical analysis of waves, which can preliminarily deal with wave slamming of complex models. Guo (Guo et al., 2020) proposed a versatile tool based on conditional probability to evaluate the interference of wave impact loads among different components. Ding (Ding et al., 2021) studied the stability of breakwaters using Fluid-Porous-Solid coupling model. The breakwater stability depends on the thickness and slopes of the porous layer. Wei (Wei et al., 2022) simulated the effect of wave impact pressure on the front bottom of the elevated box structure and used as the dataset to investigate the horizontal and vertical impact pressure distribution. Ha (Ha et al., 2020) studied the characteristics of wave impact loads and the effect of associated bubbles on vertical circular cylinders. Guo (Guo and Xiao, 2019) estimated the slamming impact loads of breaking waves on cylinders and showed the abnormal flow patterns and interactions between the breaking waves and the model cylinder. The slamming of floating wind turbine has hardly been studied.

The early research about freak waves mainly uses the potential flow theory which ignores the viscosity of fluid and imposes certain

* Corresponding author.
E-mail address: zhiming.yuan@strath.ac.uk (Z.-M. Yuan).

https://doi.org/10.1016/j.oceaneng.2022.113464
Received 10 August 2022; Received in revised form 14 December 2022; Accepted 17 December 2022
Available online 31 December 2022

restrictions on the expansion of the order of free surface. These reductions limit the accurate simulation of freak waves. In recent years, CFD method based on viscous flow theory has been widely proposed. The CFD method successfully avoids the disadvantages of potential flow theory. It can accurately simulate the wave breaking, rolling, climbing and other phenomena occurring when slamming on structures. Zeng (Zeng et al., 2022a)proposed a novel method to generate freak wave by inserting an extreme wave into a carrier wave train in time domain. The advantage of the proposed method is that the other waves can be maintained very well when modulating the profile of freak wave. Xia (Xia et al., 2015) used the nonlinear fourth-order Schrödinger equation to simulate the generation of freak waves in a 2-dimensional random sea state characterized by the JONSWAP spectrum. The evolution of the freak waves in deep water are analyzed. Structural response has become a research hotspot in recent years because of the strong destructive power of freak waves on offshore platforms. Qin (Qin et al., 2017a) made an advanced numerical study of the green water phenomena caused by freak waves. Hydroelastic effect during the green water process is considered through a fully coupled fluid-structure interaction method. Chang (Chang et al., 2021) simulated and discussed the dynamic response of TLP in freak waves considering the effects of second-order wave forces and focusing position. Second-order wave loads significantly amplify responses of the TLP in freak wave. Luo (Luo et al., 2022) conducted experiments to examine the impact and impact patterns of freak waves on the floating platform under various air-gap conditions. Qin (Qin et al., 2017b) considered the local fluid-structure interaction through a fully coupled method during the freak wave-entery impact. The differences of impact caused by a nonlinear freak wave and a regular wave are revealed. Zhang (Zhang et al., 2022) has studied the mechanism of green water events caused by freak waves. The effects of freak wave parameters and breaking waves are analyzed. It is possible to predict the freak wave with the progress of program algorithm. Doong (Doong et al., 2018) proposed a data-driven warning model based on an artificial neural network (ANN) , which is proposed to predict the possibility of freak wave occurrence. The accuracy rate (ACR) exceeds 90% and the recall rate (RCR) exceeds 87%, demonstrating the accuracy of the proposed model. Kagemoto (2022) showed that in a water-surface wave train, the peak height of a next-coming wave can be forecasted fairly well with recurrent neural networks (RNN). The industry and research communities have highlighted the occurrence of the freak wave and the severity of the associated hazards to marine structures, as well as raised the importance of taking freak waves into account in design. However, until now there has been little consensus on the physics and occurrence probability of freak waves (Bitner-Gregersen and Gramstad, 2016). Zeng (Zeng et al., 2022b) gave the occurrence probability of freak waves generated using the superposition model is obtained based on which a method is developed to determine the number of wave components of the focusing wave train. The probability based superposition model reduces energy proportion of the focusing wave train, and improves the simulation efficiency of freak waves based on the superposition model. By comparing simulated freak waves with the sea state of Japan and freak waves recorded in the laboratory, the effectiveness of the probability based superposition model is verified. Liu (Liu et al., 2022) simulated the green water and slamming loads of ship advancing in freaking wave by using the finite volume method as a CFD analysis method. To verify the accuracy of the numerical simulation method, the physical experiments and numerical simulation in the regular waves were compared, at the same time, the numerical simulation values and theoretical values of freak waves also were compared.

Above all, the damage caused by wave slamming of freak wave is much greater than the damage caused by wave slamming of conventional random wave. However, there are few studies on the impact of freak wave on floating wind turbine. In this paper, the combined wave focusing model is adopted to obtain the classical freak waves, which is of more practical significance to investigate the characteristics of floating wind turbine in freak waves. Combined numerical simulation with experiment, the wave slamming characteristics of the floating wind turbine under freak waves are studied. A set of floating wind turbine wave slamming CFD model is established in the numerical tank. The numerical model of the tank and the floating wind turbine system is modified. A typical freak wave is created in a numerical tank by the combined wave focusing model. The distribution characteristics of local slamming pressure of floating wind turbine under the action of freak wave are studied by the established freak wave model. The study can provide reference for the design of floating wind turbine under the effect of freak waves.

2. Numerical wave tank

2.1. Governing equations and discrete methods

The mathematical model of the numerical wave tank is composed of continuity and N–S equations. The continuity equation is as follows:

$$\frac{\partial \rho}{\partial t}+\frac{\partial(\rho u_i)}{\partial x_i}=0 \quad (i,j=1,2,3) \tag{1}$$

The N–S equation is as follows:

$$\frac{\partial(\rho u_i)}{\partial t}+\frac{\partial\left(\rho u_i u_j\right)}{\partial x_i}=\frac{\partial}{\partial x_j}\left[\mu\left(\frac{\partial u_i}{\partial x_j}+\frac{\partial u_j}{\partial x_i}\right)\right]-\frac{\partial p}{\partial x_i}+\rho f_i(i,j=1,2,3) \tag{2}$$

where ρ is the fluid density, p is the fluid pressure, μ is the dynamic viscosity coefficient, fi is the mass force, ui is the velocity component of the fluid particle in the i direction, and t is the time.

Considering the physical objects and related environmental conditions examined in this study, the K-ω turbulence model is adopted. The controlled return of the flow field is discretized using the finite volume method. The convection and diffusion terms are discretized through the second-order upwind scheme. Finally, the Semi-Implicit Method for Pressure-Linked Equations (SIMPLE) algorithm is used to modify the pressure and velocity fields.

2.2. Free liquid level tracking method

The free liquid surface tracking method forms the desired free liquid surface shape through dynamic mesh technology. Volume of fluid (VOF) method is used to track the change of free liquid surface, which can effectively simulate the influence of complex geometry and broken waves. The ratio of the space occupied by the fluid to the mesh space in the liquid surface attachment is C. The free surface is constructed and tracked according to the function of C at each moment to determine the position and shape of the free surface. The equation that the function of C satisfies is as follows:

$$\frac{\partial C}{\partial t}+u\frac{\partial C}{\partial x}+v\frac{\partial C}{\partial y}+w\frac{\partial C}{\partial z}=0 \tag{3}$$

From the above equation, as long as the values of C in each mesh are solved, the free liquid surface shape of the fluid at any time can be traced according to the values in each mesh.

Equation (3) is a VOF equation, which can be divided into the following three cases according to different values of C:

(1) $C=1$: the mesh is filled with fluid, which is called fluid mesh.
(2) $0<C<1$: the mesh is partially filled with fluid, which is called interface mesh.
(3) $C=0$: the mesh without fluid is called empty mesh.

2.3. Numerical simulation theory of freak waves

In this study, the combined wave focusing model is used to generate irregular waves by superimposing sinusoidal waves with different am-

plitudes, phases, and circular frequencies. Based on the wave model proposed by Longuet-Higgins, the free-surface elevation is expressed as follows:

$$\eta(x,t)=\sum_{i=1}^{N}A_i\cos(k_ix-\omega_it+\varepsilon_i) \tag{4}$$

where ki , ωi, and εi are the wave number, circular frequency, and initial phase of the i-th wave, respectively. N is the number of wave components.

In Equation (4), Ai is the i-th component wave amplitude, which can be obtained from the wave spectrum, and its expression is as follows:

$$= \tag{5}$$

where $S\eta$ is the power spectral density of random waves in the frequency domain, which is a function of the frequency ω. In this study, the International Towing Tank Conference (ITTC) spectrum is used to describe the characteristics of the random wave. $\widehat{\omega}_i$ is an estimate of ωi.

In the limiting wave focusing model, the energy is concentrated in the focusing region. However, the wave surface in the non-focusing region is almost zero, which is quite different from the actual wave surface. The occurrence probability of this phenomenon is extremely low. When the wave meets the minimum criteria ($Hmax/Hs = 2.2$), the occurrence probability of freak waves is low. To improve the efficiency of obtaining freak waves, the combination model of extreme wave random waves proposed by Zhao (2008) was applied to achieve the generation of freak waves. The expression of the combination model is as follows:

$$\begin{aligned}\eta(x,t)=&\left(1-E_p\right)\sum_{i=1}^{N}A_i\cos\left(k_i\left(x-x_p\right)-\omega_i\left(t-t_p\right)\right)\\&+E_p\sum_{i=1}^{N}A_i\cos\left(k_i\left(x-x_p\right)-\omega_i\left(t-t_p\right)+\varphi_i\right)\end{aligned} \tag{6}$$

In Equation (6), Ep is the energy ratio coefficient. When Ep is 0, it is the extreme wave model. When Ep is 1, it is the random wave model. The distribution of spectral energy in freak wave simulation can be adjusted by changing the values of Ep. In this study, when freak waves are generated, the energy ratio coefficient of 0.4 is determined to generate corresponding waves. φ_i is the random phase, which is the random number between 0 and 2π. The first term of Equation (6) determines the time and position of freak waves, and the second term determines the appearance of random waves.

2.4. Push-type wave making theory

The wave generation method of the push pedal is used in the simulation experiment. The main principle is to define the velocity inlet as the wall surface and transform the wave velocity into the movement speed of the wall mesh which is realized by the dynamic mesh technology of STAR-CCM+. The periodic reciprocating movement of the wall mesh along the wave direction push the fluid to generate waves.

The wave-building motion equation of the push pedal is as follows:

$$U_0(t)=\frac{\omega_i}{Tr(\omega_i)}\eta(x,t) \tag{7}$$

where $Tr(\omega i)$ is the transfer function between the i-th component cosine wave and the velocity of the wave-making plate, which is expressed as follows:

$$Tr(\omega_i)=\frac{4\sinh^2(k_ih)}{\sinh(2k_ih)+2k_ih} \tag{8}$$

where h is the water depth of the tank.

The wave surface equation of freak wave is substituted into Equation (7) to obtain the velocity signal of the wave-making plate:

$$\begin{aligned}U_0(t)=&\left(1-E_p\right)\sum_{i=1}^{N}\frac{\overline{\omega}_i\sqrt{2S_\eta(\widehat{\omega}_i)\Delta\omega}}{Tr(\overline{\omega}_i)}\cos\left(-\overline{k}_ix_p-\overline{\omega}_i\left(t-t_p\right)\right)\\&+Ep\sum_{i=1}^{N}\frac{\overline{\omega}_i\sqrt{2S_\eta(\widehat{\omega}_i)\Delta\omega}}{Tr(\overline{\omega}_i)}\cos\left(-\overline{k}_ix_p-\overline{\omega}_i\left(t-t_p\right)+\varphi_i\right)\end{aligned} \tag{9}$$

In the simulation of push pedal wave making, the plate only translates in the X direction. The motions in other degrees of freedom are zero.

3. Establishment and validation of a numerical model

3.1. Characteristics of the typical floating wind turbine structure

The floating wind turbine model used in this study is an X30 platform developed by X1 Wind (https://www.x1wind.com/projects/scale-prototype-in-the-canary-islands-pivotbuoy/). The typical float wind turbine has no tower tube. Steel consumption is greatly reduced. The Levelized Cost of Energy is reduced by 50% compared with the conventional floating wind turbine (Carlos, 2021–10). The typical characteristics of the typical floating wind turbine are as follows: The column and the buoy provide sufficient buoyance to meet the requirement of stability. The ballast is used to adjust the draft of the wind turbine. The whole system adopts symmetrical spread mooring, which enhances the stability of the floating foundation and reduces the weight by more than 50%.

According to the effective section scale of the tank, wave generating capacity, floating wind turbine model size, and wave design conditions, A model scale ratio of 1:50 was determined for this experiment. Fig. 1shows the set of origin coordinates and the model of the floating wind turbine. Table 1 shows the model values of the main parameters of the floating wind turbine.

3.2. Setting of monitoring points

The slender structure of the floating wind turbine, such as the horizontal and diagonal braces can be easily damaged by wave slamming impact. Several monitoring points are set on the horizontal and diagonal brace to study the slamming characteristics. According to the symmetry and location characteristics of the model, the influence of different wave directions on the wave-front surface and the wave side surface of the floating wind turbine is considered. The monitoring points H1–H4 and D1–D4 are set on the horizontal brace. The monitoring points X1–X3, A1–A3, and B1–B3 are set on the diagonal brace. The monitoring points L1–L4 and R1–R4 are set on the column. Ten monitoring points are used in the test experiemnt. However, due to the length of the article, only four monitoring points required by the article are given here. The monitoring points I1–I4 are set up to compare experimental and numerical simulation results. Fig. 2 depicts the locations of all monitoring points. Table 2 shows specific coordinates.

3.3. The numerical tank setup and verification

3.3.1. Wave generation and elimination in the numerical tank

An additional damping term in the wave height direction is added to the momentum equation of the numerical tank bank in the range of double or triple wavelengths. A long-term stable wave field can be obtained by adding a damping term, and the influence of wave reflection on wave generation at the entrance is reduced. Fig. 3depicts the division method of the numerical tank. The total length of the wave generation area is 400 m. The total length of the wave elimination area is 300 m. In addition, Euler multiple flows with a constant density are set in the depth direction of the tank. The material above the free liquid surface is defined as air, and the material below the free fluid surface is defined as water.

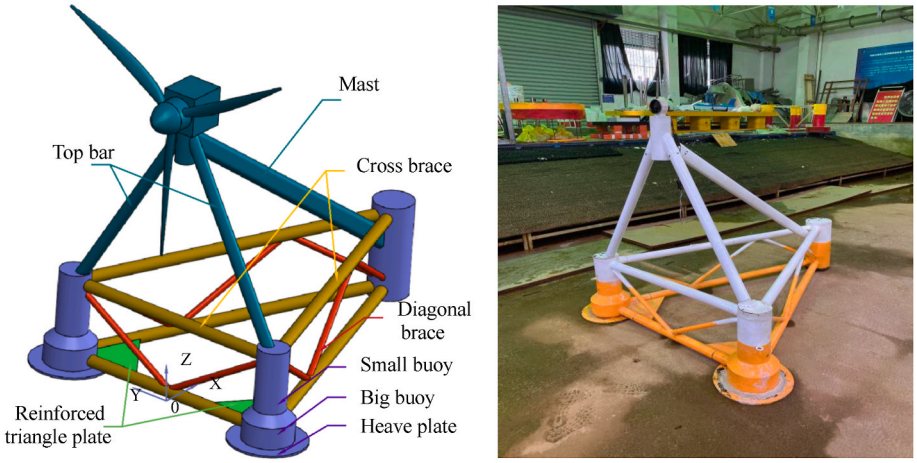

(a) Coordinate origin setting. (b) Floating wind turbine test model.

Fig. 1. Conceptual model and experimental model of floating wind turbine.

Table 1
Main particulars of the model-scale platform.

Parameter	Value
Floating body length (m)	1.8
Floating body width (m)	1.29
Floating body high (m)	0.49
Top bar length (m)	1.2
Mast length (m)	1.6
Diameter of small buoy (m)	0.16
Diameter of big buoy m)	0.21
Diameter of heave plate (m)	0.4
Reinforced triangle plate length (m)	0.4
Displacement (kg)	46
Draught (m)	0.29
The center of gravity values of x (m)	0.54
The center of gravity values of y (m)	0
The center of gravity values of z (m)	0.24

3.3.2. Computational domains and mesh generation

The centroid coordinate of the floating wind turbine is 240 m away from the entrance of the computing domain. The overlapping mesh (chimeric mesh) technology is used to automatically mesh the computing domain containing the floating wind turbine. To accurately simulate the change of free liquid surface around the structure when the floating wind turbine is in contact with the waves, local mesh refinement was carried out for the free liquid surface and key sensitive parts of the wind turbine. In the numerical simulation, the motion encryption area should be set to encrypt the possible motion range of the wind turbine, as shown inFig. 4. With this method, the wind turbine will not produce large residuals because of the change of mesh density in violent motion. Table 3 presents the specific mesh size of numerical calculation.

3.3.3. Mooring system design

The 304 stainless steel is selected as the material of mooring cable. The tensioned mooring cables are arranged symmetrically on the front and back wave surfaces of the floating wind turbine, the cable angle is 10°, anchor radius is 300 m and the length of the six mooring cables is 305 m. Each anchor chain maintains a tensioned condition and has a specific pre-tension; the water depth is 45 m. The mooring cable's length equals the linear distance between the anchor point at the bottom of the sea and the guide hole at the floating wind turbine column and buoy, plus a 1 m safety buffer. The specific parameters of the anchor chain material are shown in Table 4. The design parameters of the floating wind turbine mooring system are shown in Table 5.

The wave slamming characteristics of 0°, 45° and 90° waves is studied in this chapter, the layout of mooring systems with different wave angles and the coordinates of floating wind turbine, as illustrated in Fig. 5. 0°, 45° and 90° represent the angle between the wave direction and the y-axis of the floating wind turbine. The specific coordinates of

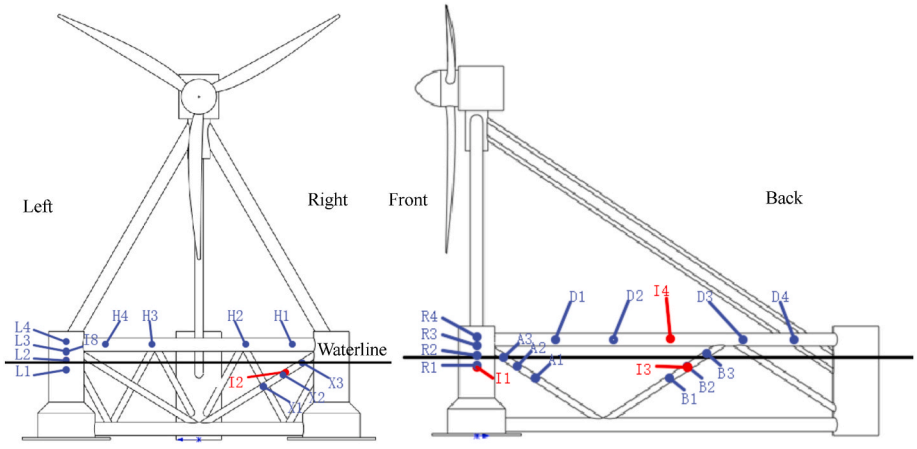

(a) Front view. (b) Side view.

Fig. 2. Location of monitoring points.

Table 2
Coordinates of monitoring points.

Point	X (m)	Y (m)	Z (m)	Note	Point	X (m)	Y (m)	Z (m)	Note
L1	−4	30	15	Slamming pressure of column	R1	0	−34	15	Slamming pressure of column
L2	−4	30	17		R2	0	−34	17	
L3	−4	30	19		R3	0	−34	19	
L4	−4	30	21		R4	0	−34	21	
H1	−1.50	−20	21.50	Slamming pressure of cross brace	D1	18.90	−25.62	21.5	Slamming pressure of cross brace
H2	−1.50	−10	21.50		D2	29.63	−21.12	21.5	
H3	−1.50	10	21.50		D3	55.08	−12.12	21.5	
H4	−1.50	20	21.50		D4	67.81	−7.62	21.5	
A1	15.63	−25.27	11.44	Slamming pressure of diagonal brace	B1	42.29	−15.84	12	Slamming pressure of diagonal brace
A2	11.74	−26.64	13.98		B2	46.47	−14.37	14.73	
A3	7.85	−28.02	16.53		B3	50.64	−12.89	17.46	
X1	−0.75	−13.68	11.44	Slamming pressure of diagonal brace	I1	0.0	−34.0	14.5	Compare experimental and numerical simulation
X2	−0.75	−17.81	13.98		I2	−0.75	−18.65	14.5	
X3	−0.75	−21.94	16.53		I3	46.12	−14.49	14.5	
					I4	42.38	−16.6	21.5	

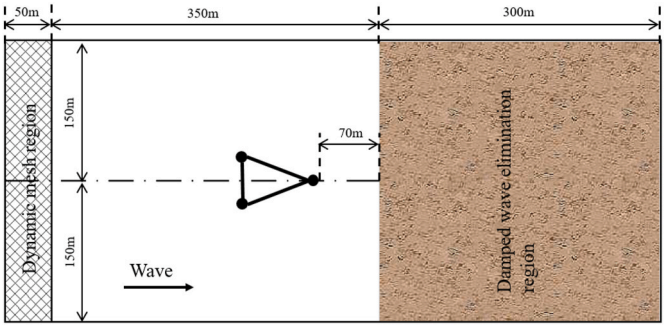

Fig. 3. Parameters of numerical tank.

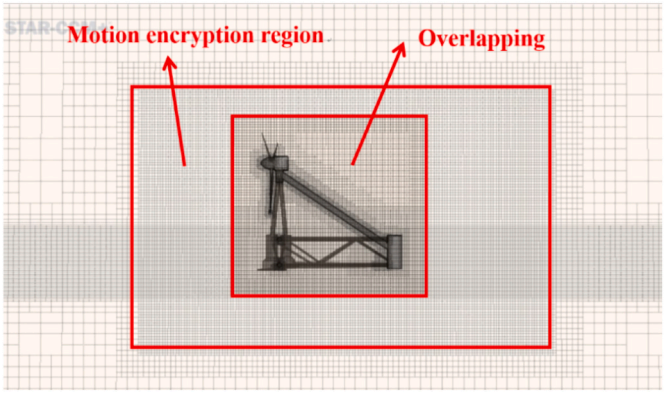

Fig. 4. Overlapping mesh and motion encryption region.

the anchor points and mooring points of the wind turbine mooring system under each wave direction are shown in Tables 6–8 respectively.

3.3.4. Mesh convergence verification

Attenuation will seriously affect the calculation accuracy, resulting in a very large calculation error.

3.3.4.1. Verification of mesh convergence for regular waves. The wave generated in this numerical simulation is Stokes' fifth-order wave, which requires high mesh accuracy. Moreover, the change in mesh size has a great influence on wave attenuation. Amongst mesh parameters, the setting of base size has the greatest influence on the accuracy of wave calculation. Owing to the numerical simulation process, the mesh size of liquid level encryption and overlapping area changes with the change of base size.

Table 3
Mesh size.

Project	Basic size			Base size of overlapping area	
Mesh size	8 m			2 m	
Project	Minimum surface size	Maximum surface size		Minimum surface size	Maximum surface size
Mesh size	0.8 m	16 m		0.4 m	16 m
Project	The water level of encryption			Movement of encryption	Leaf blade encryption
	x	y	z		
Mesh size	4 m	4 m	1 m	2 m	0.2 m

Table 4
Mooring material.

Type	Diameter mm	Conductor weight kg/m	Axial rigidity N	Breaking strength N
304 stainless steel	95	158	9.025 × 108	9×10^6

Table 5
Mooring system parameters.

Mooring mode	Number of anchors	Anchor chain length m	Pretension force kN
Catenary type	6	305	9.13×10^7

In this convergence verification, three basic sizes of 6, 8, and 10 m are set. After automatic mesh division, the total number of grids corresponding to the three different grids is 5,335,000, 3,162,000, and 1,742,000, respectively. A wave gauge is set at 50 m and 240 m from the speed entrance. The wave-making time is approximately 120 s. The iteration time step is defined as 0.005 s, and the maximum physical iteration time is 1200 s. Fig. 6shows the result of wave simulation. From the figure, the error between the theoretical and actual values of wave height at the concerns with the base size of 6 and 8 m is very small. The theoretical value in the legend is the target wave result to be obtained. Mesh size = 6–10 m in the legend is the wave result obtained by numerical simulation. Actual value in the legend is the wave result obtained by tank test. The maximum wave amplitude by using different

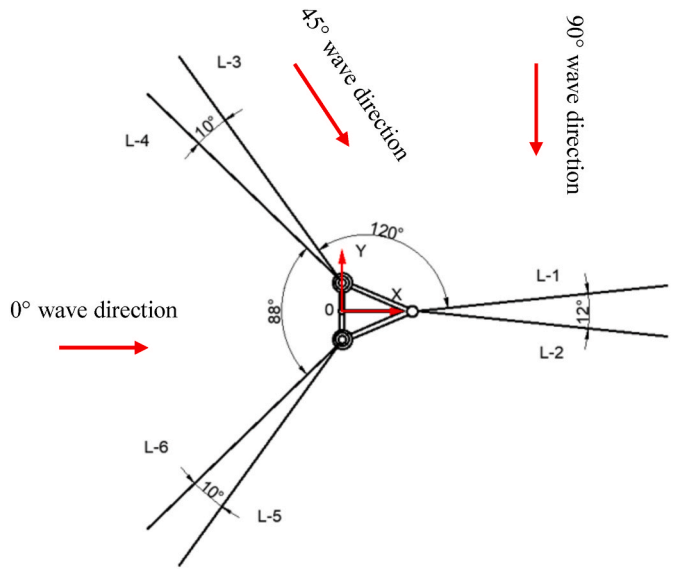

Fig. 5. Schematic diagram of mooring system with different wave direction angles.

Table 6
Anchor point and mooring point coordinates at 0°wave direction.

Chain code	Coordinates of mooring points			Anchor point coordinates		
	x	y	z	x	y	z
L-1	90	0	14.5	389.71	13.09	−50
L-2	90	0	14.5	389.71	−13.09	−50
L-3	−2.83	32.83	14.5	−205.52	254.01	−50
L-4	−2.83	32.83	14.5	−224.01	235.52	−50
L-5	−2.83	−32.83	14.5	−205.51	−254.01	−50
L-6	−2.83	−32.83	14.5	−224.01	−235.51	−50

Table 7
Anchor point and mooring point coordinates at 45°wave direction.

Chain code	Coordinates of mooring points			Anchor point coordinates		
	x	y	z	x	y	z
L-1	63.6	−63.6	14.5	284.8	−266.3	−50
L-2	63.6	−63.6	14.5	266.3	−284.8	−50
L-3	21.2	25.2	14.5	34.25	324.9	−50
L-4	21.2	25.2	14.5	8.1	324.9	−50
L-5	−25.2	−21.2	14.5	−324.9	−34.25	−50
L-6	−25.2	−21.2	14.5	−324.9	−8.1	−50

Table 8
Anchor point and mooring point coordinates at 90°wave direction.

Chain code	Coordinates of mooring points			Anchor point coordinates		
	x	y	z	x	y	z
L-1	90	0	14.5	389.7	13.05	−50
L-2	90	0	14.5	389.7	−13.05	−50
L-3	−2.8	32.8	14.5	−205.5	254	−50
L-4	−2.8	32.8	14.5	−224	235.5	−50
L-5	−2.8	−32.8	14.5	−205.5	−254	−50
L-6	−2.8	−32.8	14.5	−224	−235.5	−50

mesh sizes is shown in Table 9.

3.3.4.2. Verification of mesh convergence for slamming pressure. The measurement of slamming pressure is also impacted by the change in mesh size. The base size setting, one of many mesh settings, has the biggest impact on how accurately waves are calculated. The setting of base size, one of numerous mesh factors, has the biggest impact on the measurement accuracy of slamming pressure. Owing to the numerical simulation process, the number of grids and overlapping areas of the wind turbine model change with the change of the base size. The measurement accuracy is directly impacted by the number of grids in the wind turbine model, which immediately influences the number of grids nearby.

In this convergence verification, three basic sizes of 6 m, 8 m and 10 m are set. After automatic grid division, the total number of grids corresponding to the three different grids is 5,335,000, 3,162,000, and 1,742,000, respectively. The slamming pressure point is I2, the wave making time is approximately 120 s, the iteration time step is 0.005 s and the maximum physical iteration time is 120 s. Results of slamming pressure are displayed in Fig. 7. The chart shows a fairly tiny difference between the theoretical and observed slamming pressure at locations with bases between 8 and 12 m. From the figure, the error between the theoretical and actual values of slamming pressure at the concerns with the base size of 6 and 8 m is very small. The theoretical values in the figure are the experimental slamming results. Mesh size = 6–10m in the figure is the slamming pressure result obtained by numerical simulation. Actual value in the legend is the slamming pressure obtained by tank test.

3.3.4.3. Verification of mesh convergence for freak wave. The setting of base size, one of many mesh settings, has the greatest influence on the accuracy of wave calculation. Owing to the numerical simulation method, the mesh size of liquid level encryption and overlapping area changes with the change of base size.

In this convergence verification, three basic sizes of 6 m, 8 m, and 10 m are set. After automatic grid division, the total number of grids corresponding to the three different grids is 5,335,000, 3,162,000, and 1,742,000, respectively. A wave gauge is set at 240 m from the speed entrance. The wave-making time is approximately 600 s. The iteration time step is defined as 0.005 s and the maximum physical iteration time is 600 s. Fig. 8 shows the numerical tank with a base mesh size of 6m and 8m produced little difference in the waves. The numerical tank with a base size of 10 m produced only a small attenuation of the waves. The difference between the maximum amplitude of the wave produced by the numerical tank with an 8 m base mesh size and the highest amplitude produced by the tank with a 10 m base mesh size is 2.49%. The highest wave amplitude produced by the numerical tank with a base mesh size of 10 m is 6.21% different than the maximum wave amplitude produced by the numerical tank with a base mesh size of 12 m.

In conclusion, considering the accuracy of calculating speed and measuring slamming pressure, 8 m is used as the basic size in this study.

3.3.5. Validation of numerical wave accuracy

The accuracy of the numerical method to simulate waves is verified by comparing Stokes' fifth-order waves generated in the numerical tank with the theoretical values. The Stokes' fifth-order waves with a wave height of 8 m, water depth of 45 m, and wave period of 10 s are numerically simulated. Wave gauges are added at 50 and 240 m from the entrance of the numerical tank to monitor the wave height. Fig. 9 shows the measurement results. Stokes' fifth-order waves generated in the numerical tank agree with the theoretical curve. Thus, the numerical simulation method is reasonable. The mesh convergence is good in the calculation time. No wave attenuation phenomenon occurred.

3.3.6. Verification of freak wave

The determination of freak waves shall meet the following three criteria:

(1) The ratio of the maximum wave height to the significant wave height is greater than or equal to 2.

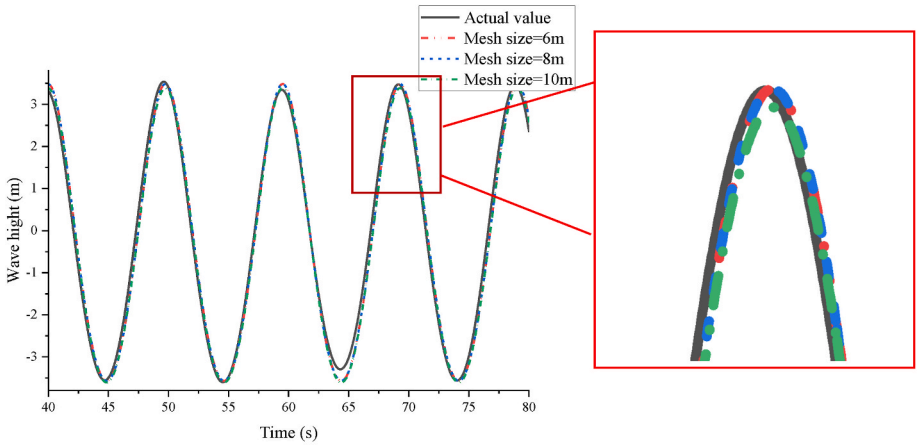

(a) Wave gauge 1

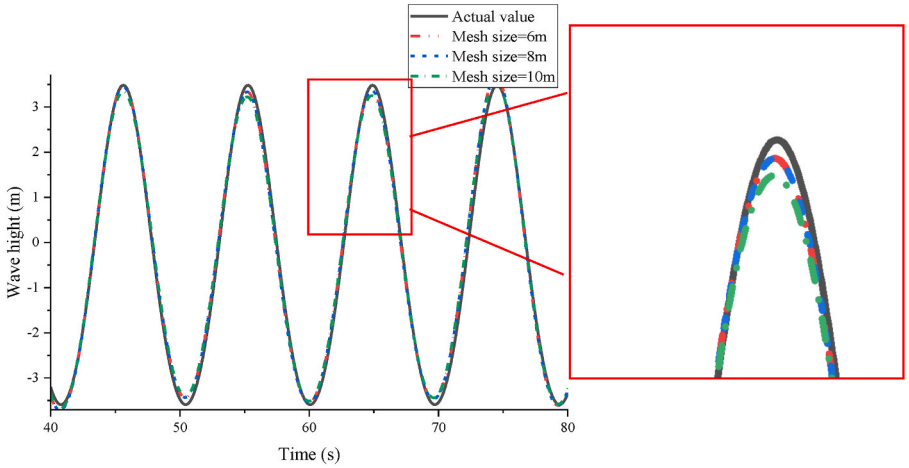

(b) Wave gauge 2

Fig. 6. Time history of the wave height.

Table 9
Maximum amplitude for different mesh base sizes.

Mesh size	Mesh = 6 m	Mesh = 8 m	Mesh = 10 m
Maximum amplitude(m)	24.11	23.51	22.05

(2) The ratio of the maximum wave height to the wave height on the left and right adjacent time series is greater than 2.
(3) The ratio of the height of the wave peak to the wave height of the freak wave is approximately 0.65.

After determining the mesh size, the floating wind turbine model and numerical wave tank are combined. The combination model of the limit

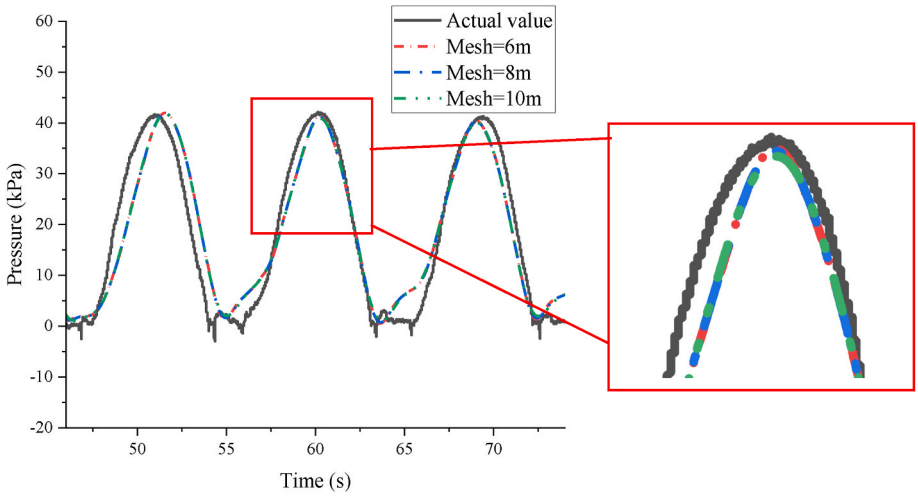

Fig. 7. Time history of the slamming pressure.

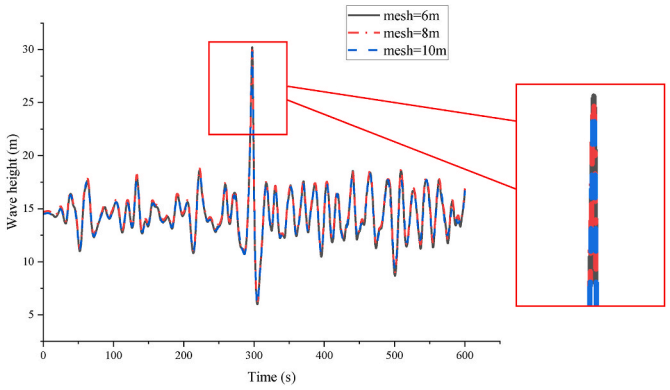

Fig. 8. Time history of wave height.

and random waves based on the ITTC two-parameter wave spectrum is selected. The push-pedal wave generation in the experimental tank is realized by using dynamic mesh technology. Fig. 10 shows the wave height time history curve monitored at the floating wind turbine position 240 m from the numerical tank to the push pedal.

According to the above three criteria, the effective wave height of the freak wave is 10.29 m, and the ratio of the maximum wave height to the effective wave height of the freak wave is 2.45. The peak value of the wave is 18.36 m. The ratio of the maximum wave height to its adjacent wave height is 2.8 and 2.58, respectively. The ratio of the peak value to the wave height is 0.73, which conforms to the definition of the freak wave.

4. Experiment test

4.1. Experiment condition

In this study, the finite element model is verified by the experimental results of the tank model test. The model test is carried out in the wind-wave-flow comprehensive tank at Jiangsu University of Science and Technology. The tank is 38 m long and 15 m wide, and the maximum effective water depth is 1 m. A multi-unit electric servo wave generator with push pedals is used to generate waves. The maximum wave height is 0.35 m. Fig. 11 shows the wind-wave-flow comprehensive tank.

Fig. 12 depicts the capacitance wave gauge and pressure sensor. A capacitive wave gauge is used in the test. The range of wave gauge is −250–250 mm, and the error is 0.5%. A CY200/CY300 series high-precision digital pressure sensor was adopted. The acquisition frequency of the pressure sensor is 1000 Hz. The Smart sensor software is directly connected to a computer to record the pressure change process. The time pressure curve is formed by this software. The 6-DOF measuring instrument is Qualisys Oqus S/N 12587, measuring frequency is 180 Hz, pixel is 4 MP and resolution ratio is 2048*2048.

The pressure sensor has a 140 m length, a diameter of 27 mm, and a minimum diameter of 7 mm. The hole diameter is 7.5 mm, the finest position of the model that needs to install the pressure sensor is 300 mm. To prevent the pressure sensor from impacting the hydrodynamic force, the majority of the pressure sensor's ends are concealed at the brace and column. After the pressure sensor is installed, waterproof adhesive is applied to prevent leakage. Part of the drilling positions and installing pressure sensors are shown in Fig. 13.

Table 10 shows the specific dimensions of the experimental model. The pretension force on the mooring line is 730 kN.

4.2. Wind load equivalent design

The wind turbine selected in this study has a full load power of 5 MW and a blade length of 98 m. Considering the cost and other factors, this experiment uses the ducted fan equivalent to the actual wind turbine. The motor and wind turbine blades above the base are simplified. The mass block is used to simulate the wind turbine mass. The load borne by the wind turbine is simulated using the ducted fan. The principle is to simplify the wind load of the wind turbine in the external environment as the reverse thrust is applied to the floating wind turbine when the ducted fan is working.

A 50-mm EDF ducted fan was selected for the experiment, and Fig. 14 shows the actual ducted fan. Fig. 15 depicts the wind speed-

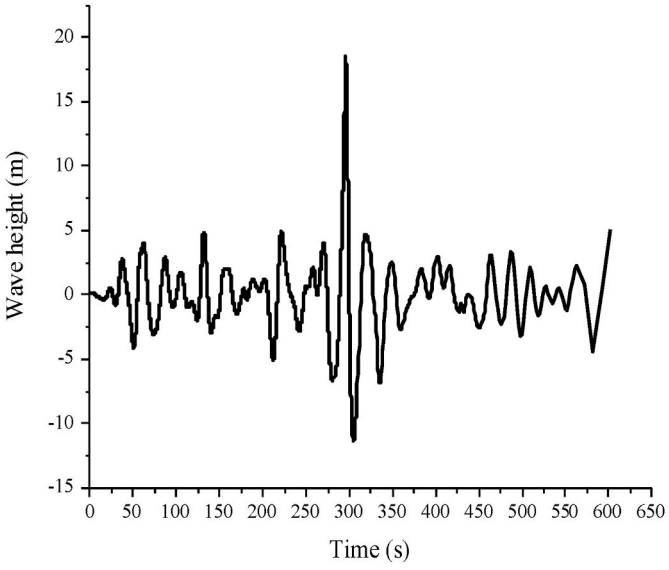

Fig. 10. Time-history of the wave height.

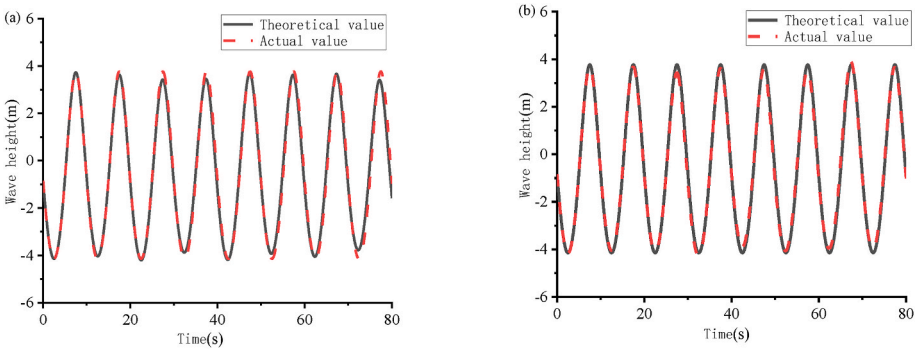

(a) Entrance (b) Central part

Fig. 9. Comparison of numerical values and theoretical values.

Fig. 11. Three-dimensional model of the floating wind turbine.

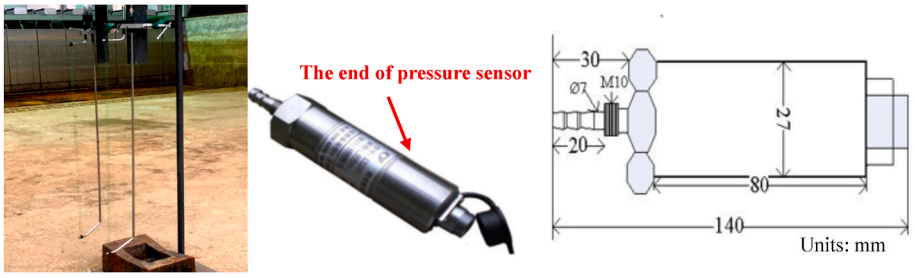

Fig. 12. Capacitance wave gauge and pressure sensor.

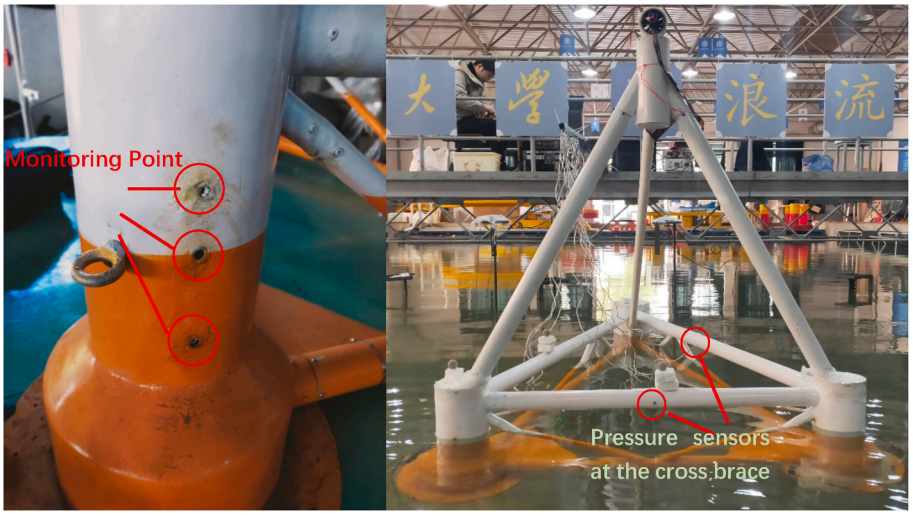

Fig. 13. The positions of the monitoring point and pressure sensors.

Table 10
Actual values of floating wind turbine.

Parameter	Unit	Real value
Floating body length	m	90
Floating body width	m	60
Floating body high	m	24.5
Top bar length	m	60
Mast length	m	80
Diameter of Small buoy	m	8
Diameter of big buoy	m	10.3
Diameter of Heave plate	m	20
Reinforced triangle plate length	m	20
Displacement	t	5713
Draught	m	14.5

thrust curve of the ducted fan. Where 0° and 45° are the wave directions of experiment. The maximum static thrust related to the test is 960 g, which is in line with the expected thrust requirements.

4.3. Free decay tests without mooring system

The error of free attenuation determines the accuracy of wave slamming distribution. In the free decay test, the initial inclination angle applied to the floating wind turbine during the measurement of pitch and roll was 10°–20°. The floating wind turbine overall sank 5–10 cm under the action of external forces during the measurement of heave. In the experiment, the experimental personnel will press the floating wind turbine down to the specified depth or tilt the specified angle, and release the restrictions on the floating wind turbine to allow it to move

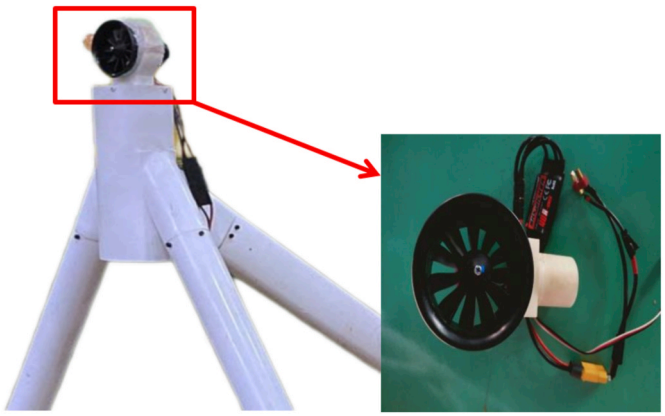

Fig. 14. Mulate the fan load.

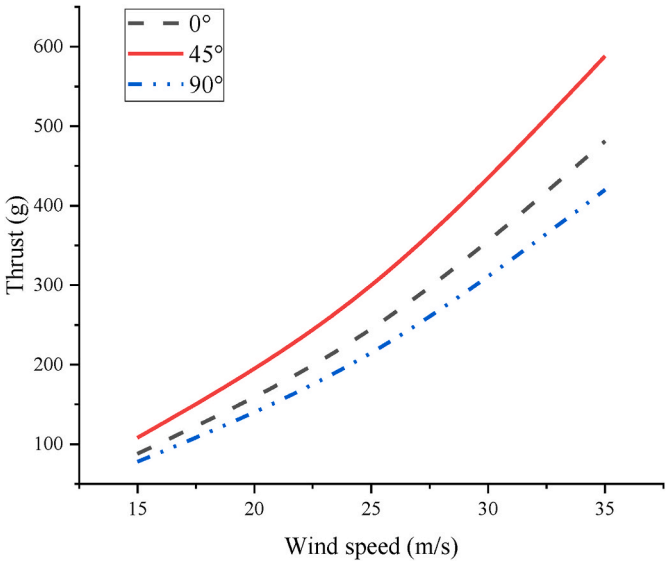

Fig. 15. NREL-5MW Wind speed - thrust curve for wind turbines.

freely. Each experiment was repeated five times, and the average value of the experimental data was taken to reduce the error. Fig. 16 shows the free decay test of physical tanks.

Fig. 17 and Table 11 show experimental and numerical results. The results show that the natural period of the floating wind turbine model in static water is close to that of the numerical simulation, and the difference is less than 3%. The accuracy of the model test parameters, such as inertia moment, gravity center, and model mass, is verified by the small error. The accuracy is ensured by the accurate model when studying the motion characteristics of the floating wind turbine.

Fig. 16. Free decay test in the physical tank.

4.4. Free decay tests with mooring system

The same experimental method is used to conduct attenuation experiments on platforms with anchor chains. The results are shown in Fig. 18 and Table 12.

4.5. Comparison between slamming pressure tests and numerical simulation results

This section selects two typical operational conditions and compares the time history curves of the pressure values measured at the same measurement point in the numerical simulation. The objective is to verify the accuracy of the finite element model in the computational fluid dynamics method and the feasibility of the analysis method. The impact period, maximum value, pressure fluctuation trend, and error range are analyzed by experimental results.

Typical operational conditions ($H = 7.5$ m, $T = 8$ s, $\beta = 45°$ wave parameters) were selected in the model test, and numerical simulation and test results at the I3 point were compared, as shown in Fig. 19 (a). The results show that: (1) I3 has an evident slamming at the position of the diagonal brace, and the numerical simulation is consistent with the experimental results in the trend of slamming pressure. (2) In the three slamming periods, the maximum values of the numerical simulation were 55, 55, and 55.5 kPa, respectively, and the maximum values of the test were 52, 53.4, and 54.5 kPa, respectively. The difference between numerical and experiment was 5.8%, 3%, and 2.4%, respectively. (3) The average period of the numerical simulation slamming pressure was 7.96 s, and the average period of the test slamming pressure was 7.91 s, which were 0.5% and 1.1% different from the theoretical value, respectively. The numerical simulation results are in good agreement with the experimental analysis results.

Typical operational conditions ($H = 7.5$ m, $T = 9$ s, $\beta = 0°$) were selected in the model test, and numerical simulation and test results at the I1 point were compared, as shown in Fig. 19 (b). The results show that: (1) The numerical simulation of the slamming pressure at I2 points was consistent with the experimental results in the trend of the slamming pressure. (2) In the three slamming periods, the maximum values of numerical results were 41.1, 40.6, and 39.7 kPa, respectively, and the maximum values of experimental results were 41.1, 41.5, and 40.8 kPa, respectively. The difference between numerical and experiment was 0.2%, 2.1%, and 2.7%, respectively. (3) The average period of the numerical simulation is 8.83 s. The average period of the test was 9.1 s, which was 1.9% and 1.1% different from the theoretical value, respectively. The numerical results are in good agreement with the experimental results.

Typical operational conditions ($H = 5$ m, $T = 6$ s, $\beta = 90°$) were selected in the model test, and numerical simulation and test results at the I1 point were compared, as shown in Fig. 19 (c). The results show that: (1) The numerical simulation of the slamming pressure at I1 points was consistent with the experimental results in the trend of the slamming pressure. (2) In the three slamming periods, the maximum values of numerical results were 73.79, 73.65, 72.88 and 73.60 kPa, respectively, and the maximum values of experimental results were 72.39, 71.72, 71.22and 71.67 kPa, respectively. The difference between numerical and experiment was 1.93%, 2.69%, 2.33%and 2.69%, respectively. (3) The average period of the numerical simulation is 9.74 s. The average period of the test was 9.68 s, which was 3.74% and 3.68% different from the theoretical value, respectively. The numerical results are in good agreement with the experimental results.

Typical operational conditions ($H = 10$ m, $T = 11$ s, $\beta = 0°$) were selected in the model test, and numerical simulation and test results at the I4 point were compared, as shown in Fig. 19 (d). The results show that: (1) The numerical simulation of the slamming pressure at I4 points was consistent with the experimental results in the trend of the slamming pressure. (2) In the three slamming periods, the maximum values of numerical results were 16.74, 17.04, and 17.48 kPa, respectively, and

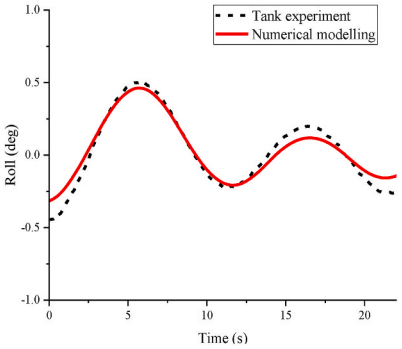

(a) Comparison of roll motion between test and numerical simulation.

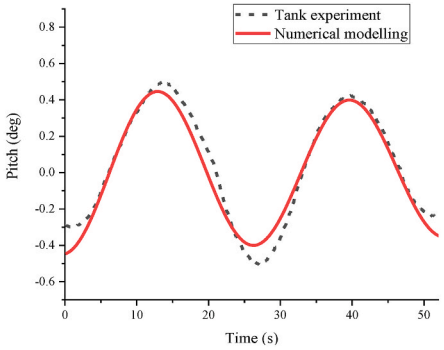

(b) Comparison of pitch motion between test and numerical simulation.

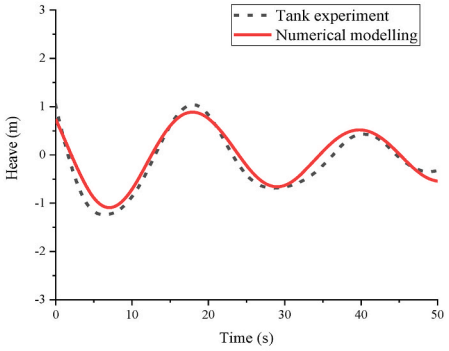

(c) Comparison of heave motion between test and numerical simulation.

Fig. 17. Tank experiments and numerical modelling comparison.

Table 11
Natural period of the platform's roll, pitch and heave motions.

Motion response	Model test	Numerical simulation	Error	Attenuation damping of tank test	Attenuation damping of numerical
Roll	10.61 s	10.84 s	2.2%	14.46%	24.27%
Pitch	26.05 s	26.7 s	2.5%	11.93%	5.37%
Heave	22.03 s	22.27 s	1.1%	25.19%	16.33%

the maximum values of experimental results were 16.02, 18.20, and 17.27 kPa, respectively. The difference between numerical and experiment was 4.49%, 6.37%, and 1.22%, respectively. (3) The average period of the numerical simulation is 9.97 s. The average period of the test was 9.97 s, which was 0.97% and 0.97% different from the theoretical value, respectively. The numerical results are in good agreement with the experimental results.

4.6. Comparison between 6 -DOF tank test and numerical simulation

In this section, a typical operational condition is selected to compare the time history curves of six degree of freedom (6 -DOF) measured by numerical simulation and experiment. The purpose is to verify the accuracy of the finite element model and the feasibility of the analysis method in the computational fluid dynamics method. According to the experimental results, the motion period, difference and error are analyzed.

In the model test, typical operational condition ($H = 5$ m, $T = 10$ s, β

Table 12
Natural period of the platform's surge, sway and yaw motions.

Motion response	Natural period
Surge	42.53 s
Sway	27.31 s
Yaw	51.15 s

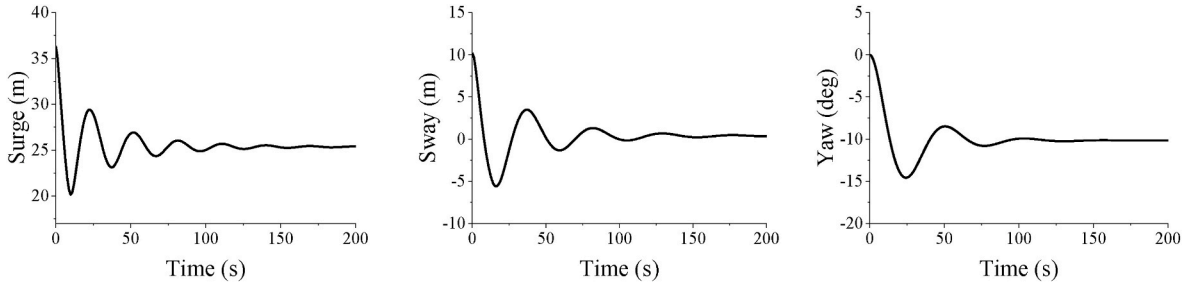

(a) Surge. (b) Sway. (c) Yaw.

Fig. 18. Free decay tests with mooring system.

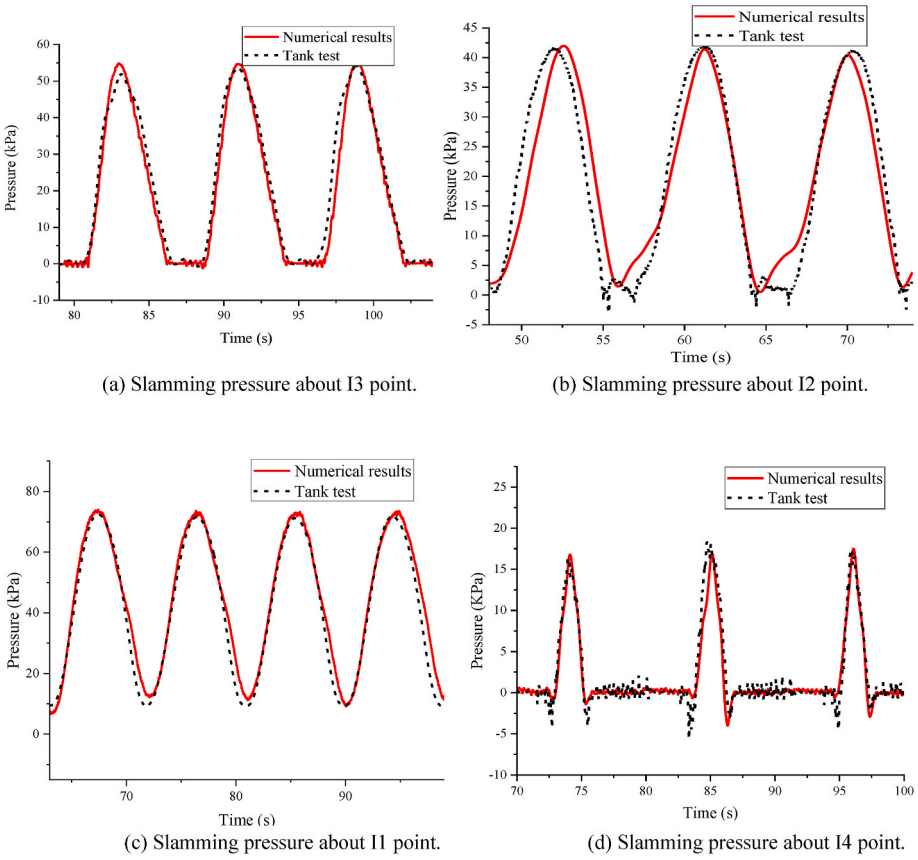

Fig. 19. Slamming pressure comparison.

= 90°) is selected, and numerical simulation of the 6 -DOF are compared with the test results. The results of 6-DOF are shown in Fig. 20.

The results show that: (1) The numerical simulation of the 6-DOF of the floating wind turbine was basically consistent with the experimental results. (2) The numerical simulation of sway, surge and heave amplitude were 3.03 m, 0.77 m and 4.42 m. The difference between numerical simulation and experimental values was 0.1%, 8% and 0.22%. The simulated roll, pith and yaw amplitudes were 3.62 m, 4.59 m and 1.50 m. The difference between numerical simulation and experimental values was 0.56%, 1.2% and 4.9%. (3) The periods of sway, surge and heave in numerical simulation were 11.40 s, 11.04 s and 11.37 s. The difference between numerical simulation and experimental values was 0.44%, 2.3% and 0.26%. The simulated roll, pith and yaw cycles were 11.22 s, 10.95 s and 11.01 s. The difference between numerical simulation and experimental values was 1%, 3.7% and 3.2%. The numerical simulation results are in good agreement with the experimental results.

4.7. Comparison of velocity tank test and numerical simulation

In this section, a typical operational condition is selected to compare the time history curves of velocity measured by numerical simulation and experiment. The purpose is to verify the accuracy of the finite element model and the viability of the analysis method in the computational fluid dynamics method. Analysis of the motion period, difference, and inaccuracy is done in light of the experimental findings.

In the model test, the typical operational condition ($H = 5$ m, $T = 10$ s, $\beta = 90°$) is selected, and the motion velocity of the buoy simulated by numerical simulation is compared with the test results. Surging, heaving, and swaying are shown in Fig. 21.

The results show that: (1) The numerical simulation of the motion speed of the floating wind turbine was basically consistent with the experimental results in the trend. However, the value of speed will fluctuate erratically due to the impact of precision in physical

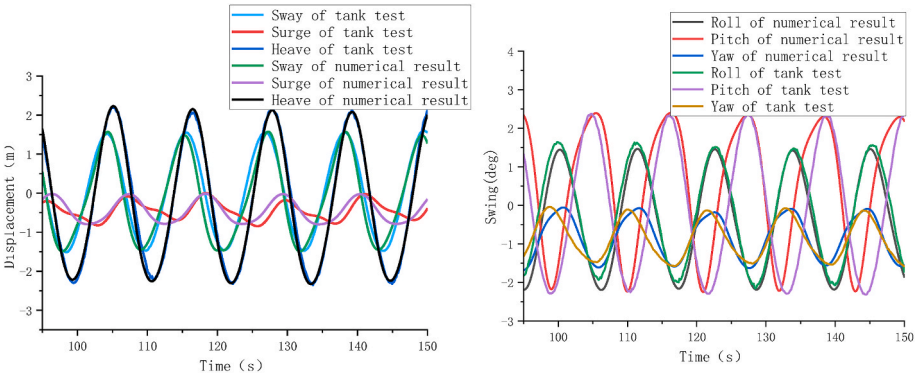

Fig. 20. 6 -DOF motion results comparison.

experiments. (2) The numerical simulation of the movement along the *y*-axis, along the *x*-axis and along the *z*-axis velocity amplitude was 18.02 m/s, 5.06 m/s and 25.14 m/s. The difference between numerical simulation and experimental values was 7.14%, 16.20%, and 4.28%. The numerical simulation of the movement around the *y*-axis, around the *x*-axis and around the *z*-axis velocity amplitude was 2.90 deg/s, 2 deg/s and 0.96 deg/s. The difference between numerical simulation and experimental values was 9.4%, 1.5%, and 15.7%. (3) The numerical simulation of the motion along the *y*-axis, along the *x*-axis and along the *z*-axis motion period was 11.17 s, 11.43 s and 11.32 s. The difference between numerical simulation and experimental values was 1.93%, 0.02%, and 0.77%. The numerical simulation results were in good agreement with the experimental results.

4.8. Analysis of motion characteristics under extreme conditions

To further study motion characteristics of the platform, the 6-DOF motion and anchor chain tension of the platform under extreme conditions are analyzed by model test. The regular wave is adopted, and the extreme condition ($H = 0.2$ m, $T = 1.7$ s) is selected. The overall motion characteristics of the platform are studied under three wave angles of 0°, 45° and 90°. The amplitude of the platform's 6-DOF motion is shown in Table 13.4. The motion duration curves of the platform's stable section are shown in Figs. 22–24 at three different wave direction angles of 0°, 45°, and 90°, respectively. It is evident that:

(1) In general, the 6-DOF motion amplitude of the 45° wave direction angle was the largest, and the pitch, surge and heave responses of the platform were larger.

(2) With respect to the platform displacement change, the surge of the platform significantly varied, with an amplitude of 102.35 mm, while the sway response did not change much from the duration curve at 0° wave direction angle. The change range of the platform swing was 8.9°, with the pitch range being the largest. The heave shift is significant and the pitch change is the most noticeable in the platform swing change at the 45° wave direction angle. From the duration curve at 90° wave direction angle, in the platform displacement, the motion amplitude and variation amplitude of heave are the largest, and the roll is largest in the platform swing change.

4.9. Nonlinear slamming loads in regular wave

In regular waves, the motion responses include both linear and high-order harmonic components. Both linear and high-order components are included in the experimental and numerical results. From the time history of motions, it can be clearly seen that the motion responses are not linear. For instance, the surge motion in Fig. 25 (a) is nonlinear, and its trough is higher than crest. However, it is well known that the motion

Table 13
6-DOF motions of the platform.

Wave direction/°	Surge/ mm	Sway/ mm	Heave/ mm	Roll/ deg	Pitch/ deg	Yaw/ deg
0	102.35	9.92	60.76	0.64	8.90	0.64
45	133.35	71.01	195.22	5.55	9.18	4.33
90	34.18	73.37	108.86	6.22	5.04	1.69

responses for the floating wind turbine platform moored by a catenary mooring system are dominated by the wave frequency components. Although the regular wave could result in high-order harmonic wave loads, these high-order harmonic components are in high frequency range, for instance, $2\omega_i$, $3\omega_i$, …, $n\omega_i$, where ω_i is the wave frequency. Considering the natural frequency of the platform in Tables 11 and 12 is larger than 10 s, those high-order harmonic loads will not induce large motion responses. The above conclusions are supported by the results of power spectral density (PSD) of motions, as shown in Fig. 25 (b) and (d), in which the incoming wave frequency is set at $T = 11.4$ s ($\omega_i \sim 0.55$ rad/s) and the wave height is 5.5 m. All the motion responses are dominated by the first-order wave frequency. The PSD of the measured pressure in Fig. 26 also shows the existence of the high-order components at $2\omega_i$, $3\omega_i$, …. However, the amplitude at those high-order components is much smaller than that at wave frequency. Since the natural frequencies at all 6-DoF are lower than the incoming wave frequency, the high-order motions induced by those high-order loads are not important, as can be seen from Fig. 25.

5. Floating wind turbine under freak waves

5.1. Freak wave result

The ITTC two-parameter wave spectrum and the limit wave-random wave combination wave focusing model are the foundations upon which the secondary development of the STAR-CCM + software is implemented. In the three-dimensional numerical tank, the freak wave is produced using the push-type wave creation theory. The wave height meter is placed 240 m away from the numerical tank to produce the wave height time domain curve, as shown in Fig. 27.

5.2. 6-DOF motions of floating wind turbine under freak waves

The floating wind turbine's 6-DOF motions in freak wave circumstances is depicted in Fig. 28. The heave is most influenced by freak slamming, according to Fig. 28 (a). When the freak wave hits, the higher wave height elevates the entire floating wind turbine, resulting in a maximum movement of 3.51 m. The second-largest impact of the freak wave on the surge is due to the freak wave pushing the entire floating wind turbine backward. The sway of the floating wind turbine is least

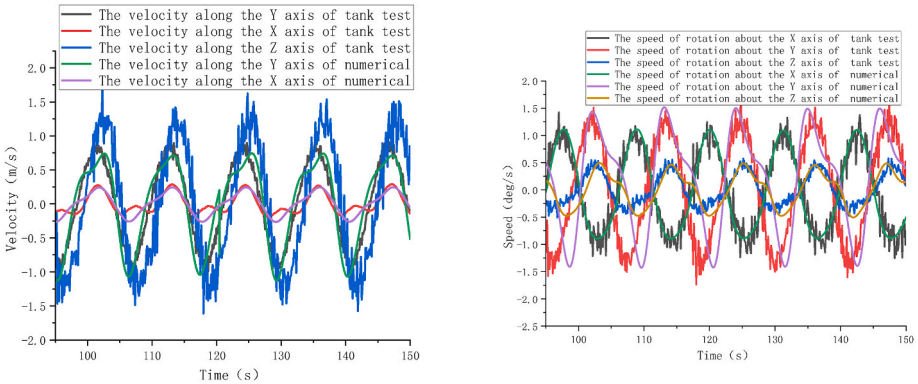

Fig. 21. Comparison of physical experiment and numerical simulation of platform velocity.

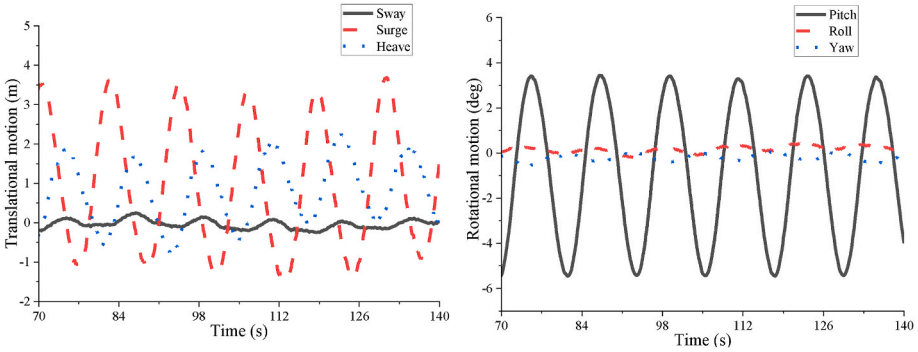

Fig. 22. Motion responses of platform at 0° wave direction.

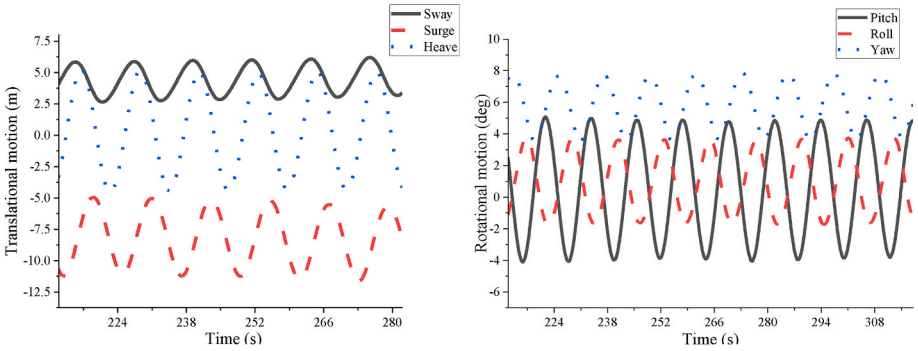

Fig. 23. Motion responses of platform at 45° wave direction.

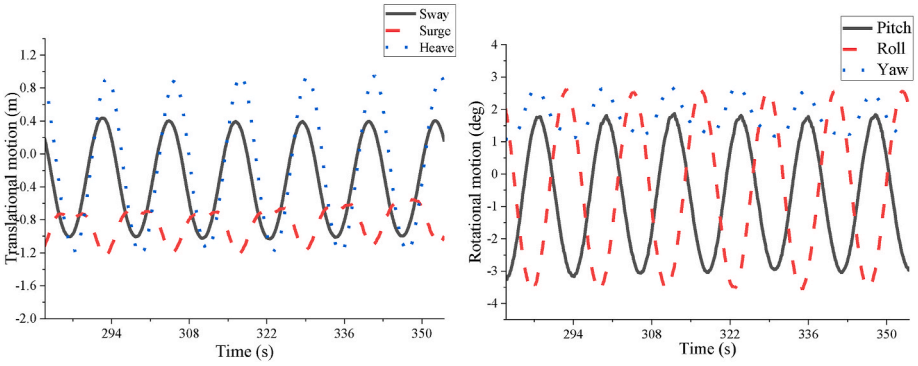

Fig. 24. Motion responses of platform at 90° wave direction.

impacted by the freak wave because its wave direction is 0°, which prevents it from shaking the turbine in the sway direction.

The pitch is most impacted by the crashing of the freak wave, as shown in Fig. 28 (b). When the freak wave impacts the structure, the floating wind turbine near the velocity intake is elevated first, followed by the portion farther from the velocity inlet, which increases pitch. Roll and yaw are essentially not affected by the freak waves because the freak wave direction is 0°, which indicates that the floating wind turbine will not move around the *x*- and *z*-axes.

5.3. Slamming load distribution of floating wind turbine under freak waves

The slamming load characteristics of columns, cross brace, and diagonal brace of the floating wind turbine are studied under freak waves generated by the numerical tank.

5.3.1. Slamming pressure distribution characteristics of columns

Fig. 29 shows the time series curve of freak waves slamming pressure on column measuring points L1–L4, which are on the wavefront surface of the floating wind turbine. Fig. 30 depicts the time series curve of freak waves slamming pressure on column measuring points R1–R4, which are on the wave side surface of the floating wind turbine. According to Fig. 29, every measuring point on the columns is subjected to severe wave slamming. The measured value of the measuring point is the pressure of static water because the measuring point L1 on the column of the wavefront surface is below the water line surface. The maximum slamming pressure point when the freak wave arrives is point L2, which is 89 kPa. Given the interaction between the wave period and the inherent period of the wind turbine, the wind turbine is subjected to multiple severe waves slamming under the loads of freak waves.

According to Figs. 29 and 30, the slamming pressure shows an evident double-peak phenomenon, which indicates that the wind turbine suffers the second severe slamming after suffering the freak wave slamming. The maximum pressure point of the second slamming is the

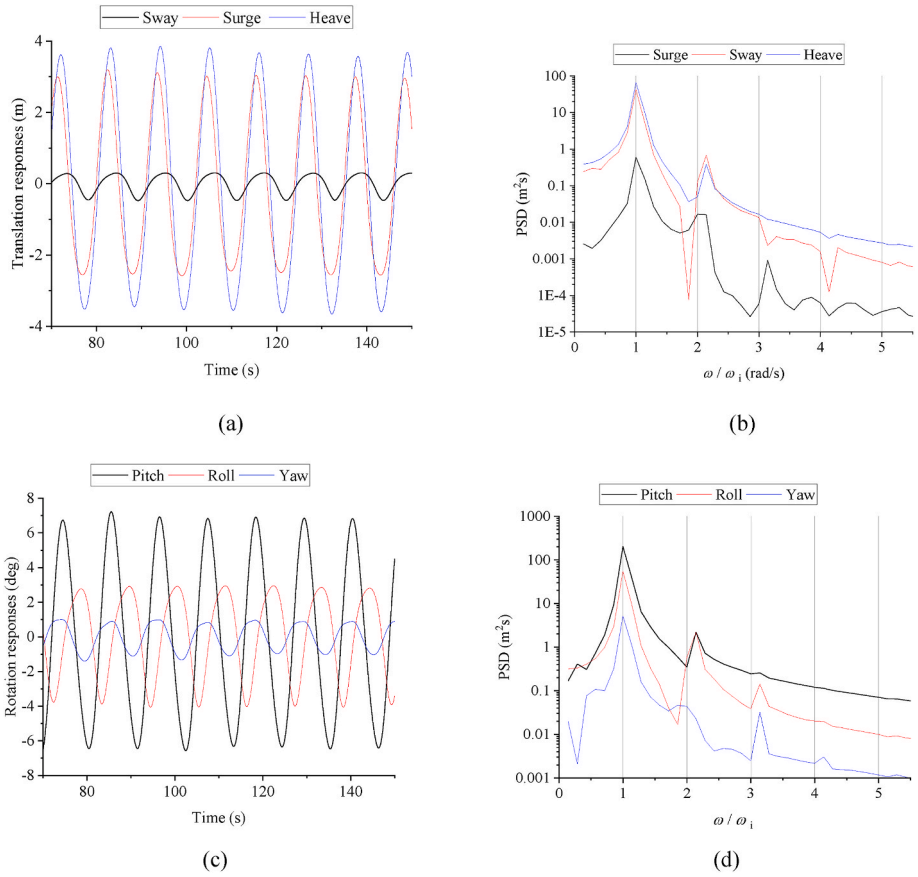

Fig. 25. Responses of 6-DoF at an incoming wave condition of $H = 5.5$ m, $T = 11.4$ s, $\beta = 90°$. (a) Time history of three translational motions; (b) PSD of three translational motions; (c) Time history of three rotational motions; (d) PSD of three rotational motions.

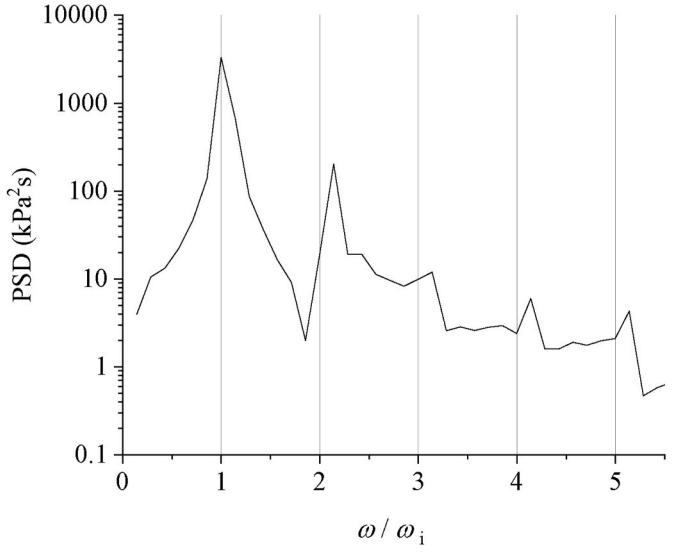

Fig. 26. PSD of slamming pressure under regular wave condition of $H = 5.5$ m, $T = 11.4$ s, $\beta = 90°$.

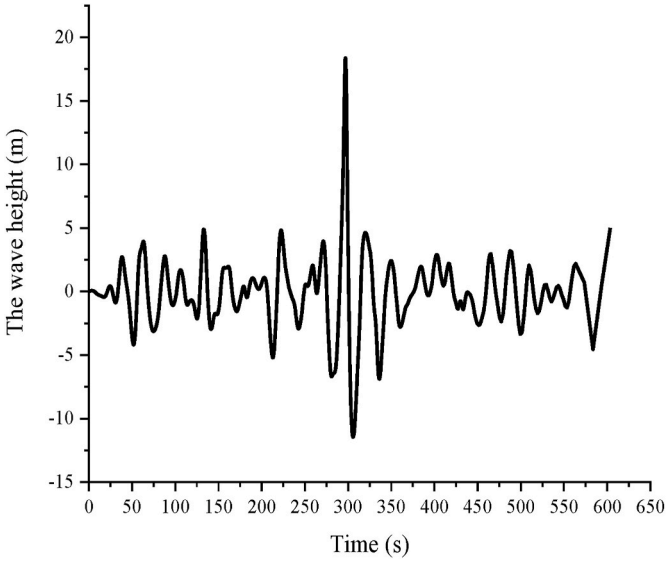

Fig. 27. Freak wave elevation.

L1 point, which is 88.6 kPa. When the freak waves pass through the floating wind turbine, the wind turbine is rapidly elevated. When the wind turbine reaches the highest position, the anchor force makes the wind turbine move downward. Then the wind turbine reaches the lowest position under the inertia effect, resulting in the wave of a small wave height has a large slamming effect on the wind turbine.

High-order responses are also observed under freak wave conditions at $H_s = 9$ m, $\omega_p = 0.3$ rad/s as shown in Fig. 31. The frequency of response is normalized by the peak frequency of the freak wave. Since the natural frequencies at all 6-DoF are much lower than the peak frequency of the freak wave, the high-order pressures induced by those high-order loads are not important.

Comparing the slamming pressure values of the columns on the

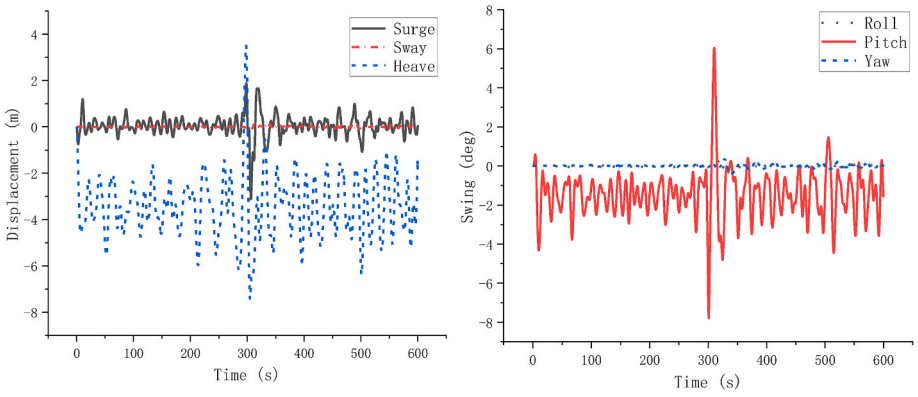

(a) Translational motions. (b) Rotational motions.

Fig. 28. 6-DOF of floating wind turbine under freak waves.

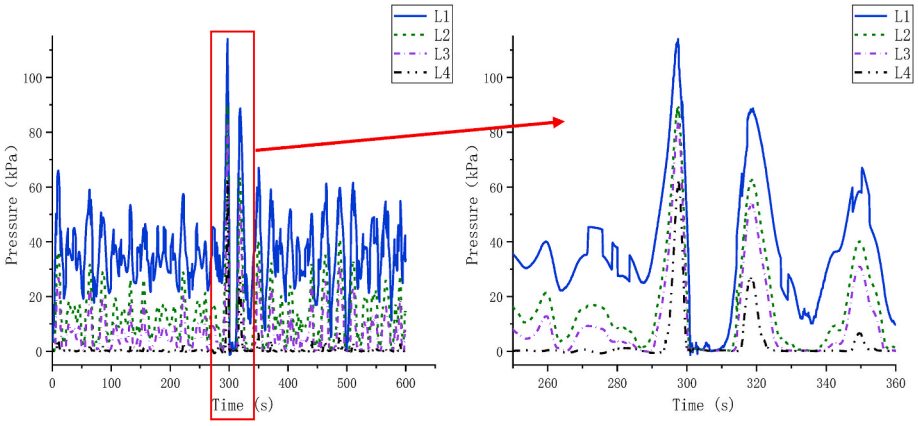

Fig. 29. The time history of wave slamming pressure on the column of the wave front surface.

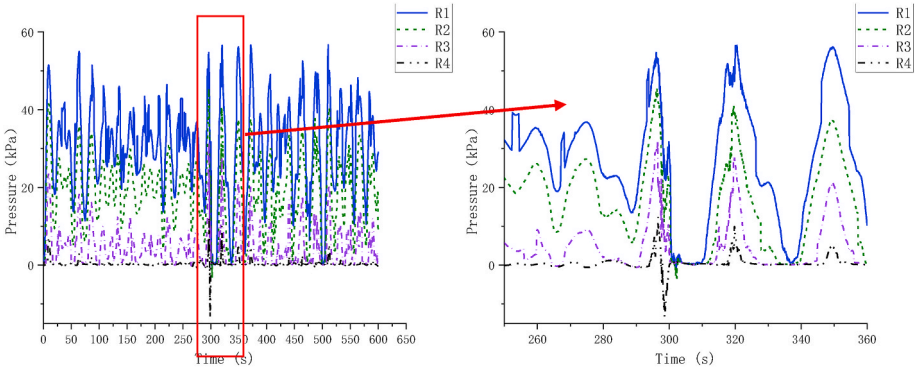

Fig. 30. The time history of wave slamming pressure on the column of the wave side surface.

wavefront surface with the wave side surface, the slamming of the column on the wave side surface is nonlinearly weaker than that on the wavefront surface. The negative pressure appears at the measuring point R4. According to Fig. 32 (a), the v phenomenon at 298.47 s makes the wave climb, and the column of the wavefront surface has greater water pressure than the column of the wave side surface. According to Fig. 32 (b) and (c), the height of the water surface on the wave side surface is significantly lower than that on the wavefront surface. The reason is the barrier of the column to waves. The structure of the floating wind turbine, particularly the column, has a strong blocking effect on the wave.

Two or three small fronts appear within a large crest when the wave is slammed because of the column. This phenomenon indicates that the blocking effect of the column on the wave is greater than the slamming effect of the freak wave on the structure. In addition, the air around the strut will produce a strong negative pressure (relative to atmospheric pressure) at the wave retreat moment after the wave slamming because the position of monitoring point R4 is very high. The suction generated by the negative pressure is combined with gravity. This condition makes the strut structure pull down and produces the suction effect. Given the wave accumulation at the same height as the positive wave upward monitoring point L4, the wave will not disappear rapidly. Therefore, no negative pressure phenomenon occurred.

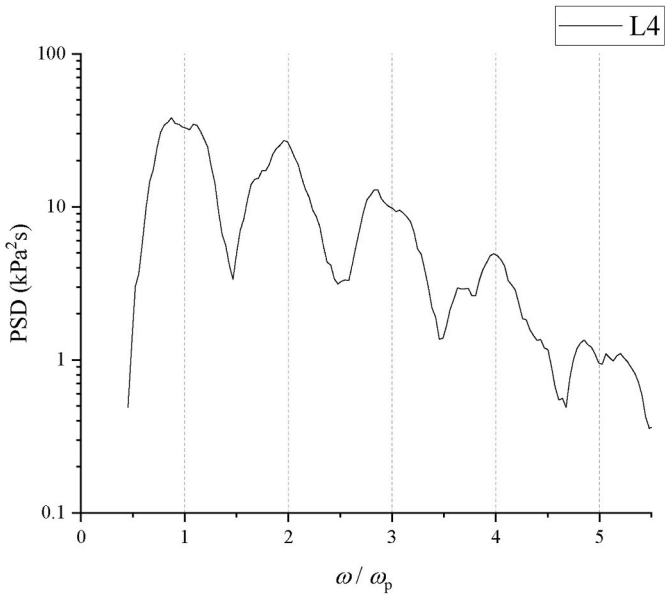

Fig. 31. PSD of slamming pressure under freak wave condition at $H_s = 9$ m, $\omega_p = 0.3$ rad/s; The cut-off frequency is set at 0.25 Hz (or $\omega/\omega_p = 0.5$).

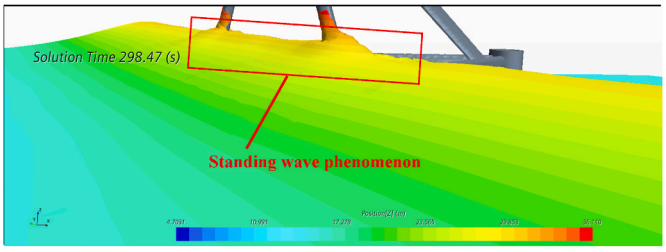

(a) t=298.47 s

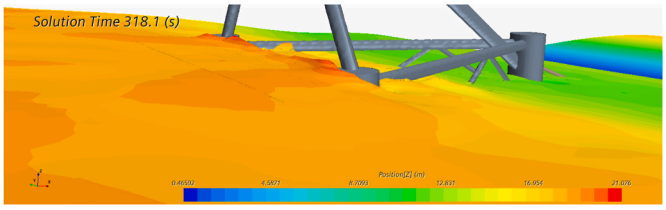

(b) t=318.1 s

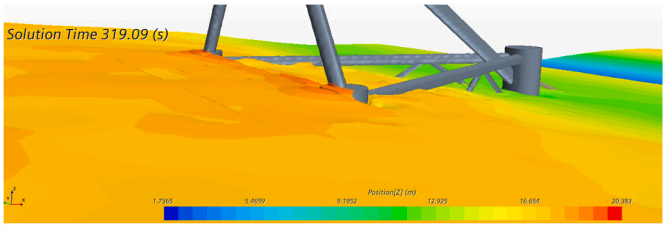

(c) t=319.09 s

Fig. 32. Wave elevation.

5.3.2. *Slamming pressure distribution characteristics of the cross brace*

The slamming pressure results of freak waves on cross brace by numerical tank are shown in Fig. 33. It can be found that due to the wave transmission factor, the time difference between the adjacent maximum slamming press Fig. 33 shows the slamming pressure results of freak waves on a cross brace by a numerical tank. Owing to the wave transmission factor, the time difference between the adjacent maximum slamming pressure points of cross brace D1–D4 is 1 s. The slamming pressure at the measuring points D3 and D4 is also reduced compared with those of the measuring points D1 and D2. The energy dissipation of the freak waves occurs in the transmission process, which weakens the wave impact at points D3 and D4. Therefore, the slamming pressure is smaller. As shown in Fig. 34, accumulation occurred at the column when the freak waves slammed. Point D4 which is closer to the column than point D3 is affected more evidently by wave accumulation. Therefore, the pressure increased accordingly.

Fig. 33 (b) shows the pressure distribution of different measuring H1–H4 points. The slamming pressure is the same. The maximum slamming pressure is 66.2 kPa. The negative pressure appeared at each measuring point on the cross brace. The maximum negative pressure is at D1, which was −16 kPa. The freak waves slamming cross brace is a transient process, and the rapid wave slamming cross brace presses the surface of the braces rapidly, resulting in a steep slamming pressure. At the end of the slamming, the air around the strut will produce a strong negative pressure (relative to atmospheric pressure) at the wave retreat moment after the wave slamming. The suction generated by the negative pressure is combined with the gravity to produce the suction effect (Min et al., 2020).

Comparing the cross brace on the wave side surface, the slamming pressure on the cross brace on the wavefront surface is greater than that on the wave side surface. The peak value of the wavefront surface is 207.8% of the peak value of the wave side surface. After the freak waves slammed, the strut on the wavefront surface had a second larger slamming than the strut on the wave side surface. However, the D1 measuring point close to the front column had a small second impact.

In addition, Fig. 33 (b) shows that the slamming pressure value of the measuring point of the wavefront surface cross brace fluctuates at the high point. The slamming period of the wavefront cross brace is 7 s, which is much higher than the 3.7 s of the side wavefront cross brace. The reason is the wave accumulation phenomenon, as shown in Fig. 32 (a). When the freak wave arrives, the wave faces the cross brace. Wave accumulation makes the liquid surface stay on the wave surface for longer than that on the side wave surface without wave accumulation, which makes the slamming period longer. If the liquid surface stays for a long time, the free liquid surface changes irregularly under the action of gravity, which makes the slamming pressure fluctuate.

5.3.3. *Slamming pressure distribution characteristics of a diagonal brace*

Fig. 35 (a)–(c) shows the slamming pressure time series curves of different measuring points on the diagonal brace. The slamming pressure on the diagonal brace increases significantly when the freak wave appears. The measuring points X1, X2, A1, A2, B1, and B2 are located below the water line, therefore, no slamming exists when the freak wave arrives. The maximum slamming pressure point when the freak wave arrives is point X3, which is 90 kPa. The pressure on the wind turbine surface plummets after the slamming of the freak wave, producing a vast "trough." At this point, the pressure of the measuring points X1, X2, and A2 has dropped to 0 kPa, indicating that the measuring points X1, X2, and A2 have been completely above the water. When the next wave passes, wave slamming will occur.

The time series curves of wave slamming pressure on the diagonal brace are in good agreement with the time series curves of the freak wave height. On the diagonal brace X and A, after the slamming pressure reached the maximum value, another larger peak appeared immediately. The slamming pressure showed a double-peak distribution. However, no double-peak phenomenon occurred on the diagonal brace B. The slamming period on diagonal brace B is shorter than that on diagonal braces X and A. The maximum wave height of the freak wave causes the maximum slamming pressure and the maximum vertical movement of the wind turbine. Meanwhile, the wind turbine begins to move in the negative direction of the Z axis. When the next wave passes the floating wind turbine, the wind turbine is at the lower position, leading to a large height difference. Therefore, the second large slamming occurs. The time series curve of slamming pressure shows a

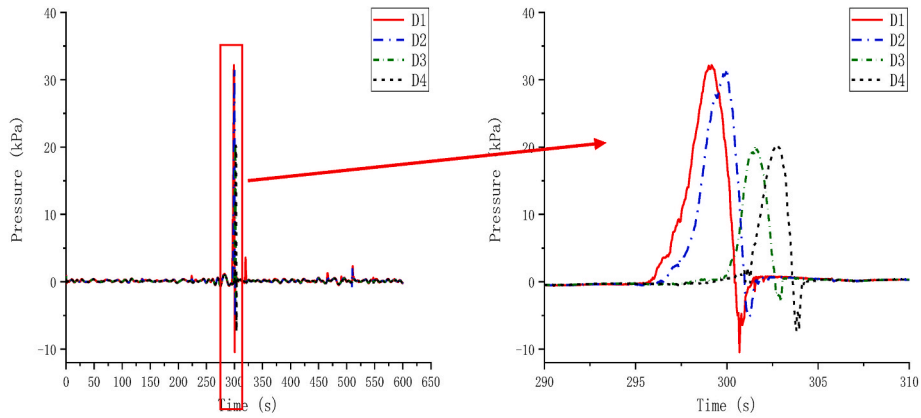

(a) Cross support measuring points D1-D4.

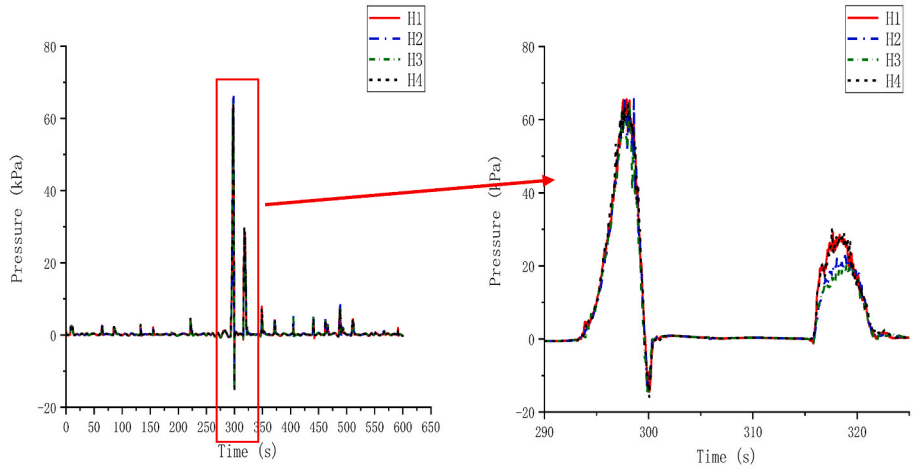

(b) Cross support measuring points H1-H4.

Fig. 33. Time history of slamming pressure at each cross brace concern.

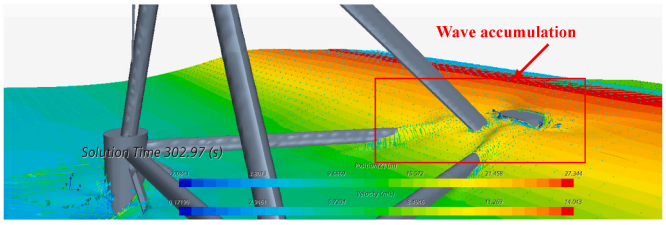

Fig. 34. Wave elevation at $t = 302.97$ s.

double-peak distribution. However, when a subsequent new wave arrives, the two columns in the upstream will be lifted first, and the position of the downstream column will move lower. Therefore, the B1–B3 diagonal brace is completely buried in the water, as shown in Fig. 36 (a). This event generates a slamming phenomenon without a wave crest. The slamming period of measuring points B1–B3 is smaller than that of measuring points X1–X3 and A1–A3. The wind turbine starts to rise under the action of buoyancy when the wave of "secondary slamming" is transmitted to the downstream B diagonal brace, as shown in Fig. 36 (b). Therefore, no double-peak phenomenon occurred on the B diagonal brace.

Fig. 35 shows that the slamming pressure value of the measurement point with negative pressure does not rise directly after reaching the lowest point compared with that of other measurement points without negative pressure, but it stays at 0 kPa for a period of time. The reason is that the measuring point with a negative pressure has been completely exposed to the air when the negative pressure occurs, and the negative pressure phenomenon is only a transient process. After the negative pressure phenomenon is over, the measuring point is still exposed to the air. A gap period exists after the end of the negative pressure phenomenon and before the wave hits the measuring point with a bang pressure of 0 kPa.

6. Conclusions

This study investigates the slamming pressure characteristics of a floating wind turbine under freak waves by combining numerical simulation with an experimental test. A set of accurate and reliable numerical models are established by using the CFD method for the wave slamming pressure of the floating wind turbine and freak wave numerical tank. The slamming pressure of the column, cross brace, and a diagonal brace of the floating wind turbine under freak waves is investigated. The following conclusions are obtained:

(1) A small difference exists between the numerical and physical models of the floating wind turbine. The maximum error of slamming pressure is 5.8%, and the average error is smaller than 3.8%. A small error verifies that the established wave slamming load analysis method is accurate.
(2) When the floating wind turbine is slammed by a freak wave, the slamming pressure on the wavefront surface is the most serious.

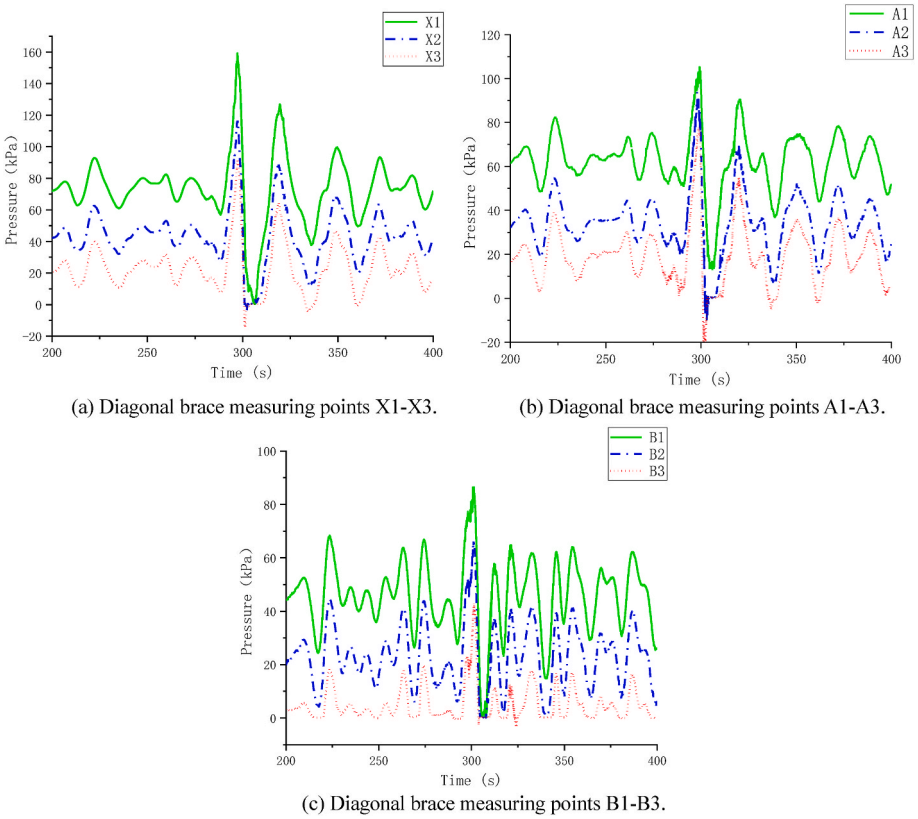

(a) Diagonal brace measuring points X1-X3.

(b) Diagonal brace measuring points A1-A3.

(c) Diagonal brace measuring points B1-B3.

Fig. 35. Time history of slamming pressure on diagonal brace.

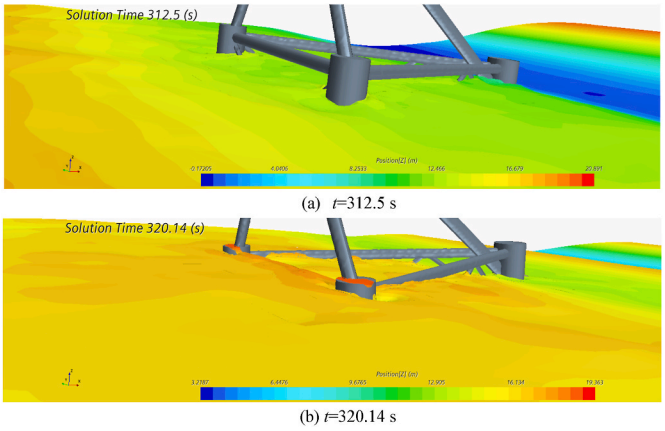

(a) t=312.5 s

(b) t=320.14 s

Fig. 36. Wave elevation.

The maximum slamming pressure of the freak wave is 89.0 kPa, which is approximately 350% of the conventional slamming pressure of 24.9 kPa. The slamming pressure generated by the freak wave on the wind turbine structure gradually decreases along the height direction.

(3) The slamming pressures at different measuring points on the column show a strong nonlinearity. Considering the coupling effect of wind turbines and wave slamming, slamming pressure presents an evident double-peak phenomenon. This phenomenon indicates that the wind turbine suffered the second severe slamming after experiencing the freak wave slamming. The maximum value of the second slamming pressure is 88.6 kPa, which increases the damage risk of the structure.

(4) For the diagonal brace, a double-peak phenomenon occurred at measuring points X1–X3 and A1–A3. However, no double-peak phenomenon was observed at measuring points B1–B3. The slamming periods of measuring points B1–B3 are smaller than those of measuring points X1–X3 and A1–A3.

CRediT authorship contribution statement

Fali Huo: Writing, Conceptualization, Methodology, and Editing. **Yupeng Zhao:** Calculation, Simulation, Writing and, Model Testing. **Jingxi Zhang:** Model Testing and Writing. **Ming Zhang:** Data Processing and Writing. **Zhi-Ming Yuan:** Conceptualization, Reviewing and Editing.

Declaration of competing interest

The authors declare that they have no known competing financial interests or personal relationships that could have appeared to influence the work reported in this paper.

Data availability

Data will be made available on request.

Acknowledgments

This work was financially supported by the National Natural Science Foundation of China (Grant No. 52071161). The support is gratefully acknowledged by the authors.

References

Baarholm, R., Faltinsen, O.M., 2004. Wave impact underneath horizontal decks[J]. J. Mar. Sci. Technol. 9 (1), 1–13.

Bitner-Gregersen, E.M., Gramstad, O., 2016. Rogue Waves: Impact on Ships and Offshore Structures. DNV GL Strategic Research & Innovation: DNV GL.

Carlos, C., 2021-10-12. X30 platform: scale prototype in the canary Islands[EB/OL]. https://www.x1wind.com/projects/scale-prototype-in-the-canary-islands-pivotbuoy.
Chang, S., Huang, W., Liu, F., et al., 2021. Influence of second-order wave force and focusing position on dynamic responses of tension leg platform under a freak wave [J]. Ocean. Eng. 242, 110126.
Ding, D., Ouahsine, A., Xiao, W., et al., 2021. CFD/DEM coupled approach for the stability of caisson-type breakwater subjected to violent wave impact[J]. Ocean. Eng. 223, 108651.
Doong, D.J., Peng, J.P., Chen, Y.C., 2018. Development of a warning model for coastal freak wave occurrences using an artificial neural network[J]. Ocean. Eng. 169, 270–280.
Faltinsen, O.M., 1990. Wave loads on offshore structures[J]. Annu. Rev. Fluid Mech. 22 (1), 35–56.
Guo, Y., Xiao, L., 2019. Lu WC FD simulations of wave impact loads on a truncated circular cylinder by breaking waves[J]. Int. J. Offshore Polar Eng. 29, 306–314, 03.
Guo, Y., Xiao, L., Lu, W., et al., 2020. Spatial distribution and interference of wave impact loads among structural components of a semi-submersible[J]. Ocean. Eng. 212, 107671.
Ha, Y.J., Kim, K.H., Nam, B.W., et al., 2020. Experimental investigation for characteristics of wave impact loads on a vertical cylinder in breaking waves[J]. Ocean. Eng. 209, 107470.
Jain, A.K., 1997. Nonlinear coupled response of offshore tension leg platforms to regular wave forces[J]. Ocean. Eng. 24, 32–37.
Kagemoto, H., 2022. Forecasting a water-surface wave train with artificial intelligence (Part 2)–Can the occurrence of freak waves be predicted with AI?[J]. Ocean. Eng. 252, 111205.
Liu, D., Li, F., Liang, X., 2022. Numerical study on green water and slamming loads of ship advancing in freaking wave[J]. Ocean. Eng. 261, 111768.
Luo, M., Rubinato, M., Wang, X., et al., 2022. Experimental investigation of freak wave actions on a floating platform and effects of the air gap[J]. Ocean. Eng. 253, 111192.
Min, L., Chan, G.K., Lee, W.X., , et al.Dominic, E.R., 2020. Experimental study of freak wave impacts on a tension-leg platform[J]. Mar. Struct. 74.
Nielsen, F.G., 2003. Comparative study on air-gap under floating platforms and run-up along platform columns[J]. Mar. Struct. 16, 97–134.
Qin, H., Tang, W., Hu, Z., et al., 2017a. Structural response of deck structures on the green water event caused by freak waves[J]. J. Fluid Struct. 68, 322–338.
Qin, H., Tang, W., Xue, H., et al., 2017b. Dynamic response of a horizontal plate dropping onto nonlinear freak waves using a fluid–structure interaction method[J]. J. Fluid Struct. 74, 291–305.
Wei, K., Zhou, C., Xu, B., 2022. Spatial distribution models of horizontal and vertical wave impact pressure on the elevated box structure[J]. Appl. Ocean Res. 125, 103245.
Xia, W., Ma, Y., Dong, G., 2015. Numerical simulation of freak waves in random sea state [J]. Procedia Eng. 116, 366–372.
Zeng, F., Zhang, N., Huang, G., et al., 2022a. A novel method in generating freak wave and modulating wave profile[J]. Mar. Struct. 82, 103148.
Zeng, F., Zhang, N., Huang, G., et al., 2022b. A novel method in generating freak wave and modulating wave profile[J]. Mar. Struct. 82, 103148.
Zhang, H., Tang, W., Yuan, Y., et al., 2022. The three-dimensional green-water event study on a fixed simplified wall-sided ship under freak waves[J]. Ocean. Eng. 251, 111096.
Zhao, X.Z., 2008. Experimental Study and Numerical Simulation of Freak waves[D]. Dalian University of Technology.